Bulletin of Earthquake Engineering
https://doi.org/10.1007/s10518-026-02417-9

ORIGINAL ARTICLE

Computational study on stiffened topology-optimized shear links for eccentrically braced frames

Yasser N. Saleh[1,2] · **Sherif A. Mourad**[2] · **Hanadi G. Salem**[3] · **Amr M. Ibrahim**[1]

Received: 10 October 2025 / Accepted: 24 February 2026

Abstract
This study presents a numerical investigation into the performance of topology-optimized shear links in eccentrically braced frames (EBFs). Stiffened variations of an X-shaped topology-optimized (TO) link were introduced, incorporating additional stiffening elements to enhance strength and energy dissipation. The optimized links were analyzed under monotonic and cyclic loading and tested numerically within full-scale EBF systems. Results demonstrated that the optimized links outperformed the conventional reference shear links (RSL-1) in multiple aspects. TO-00 and TO-01 links exhibited 22% higher base shear, with TO-01 achieving the highest energy dissipation, 31% greater than the conventional shear link over the loading history. Under cyclic loading, the baseline TO link (TO-00) recorded the highest shear strength (660 kN), surpassing RSL-1 by 34%. Stiffened links showed improved stress distribution, improving overall ductility. Additionally, the damping coefficients of TO links improved, considering previous research on TO shear links. These findings highlight the feasibility of topology-optimized shear links for seismic applications, offering a balance between superior structural performance and manufacturability.

Keywords Shear links · EBF (Eccentrically Braced Steel Frames) · Topology optimization · Cyclic loading · WAAM (Wire and Arc Additive Manufacturing)

1 Introduction

Post-earthquake reconnaissance has repeatedly demonstrated the vulnerability of conventional structural systems to severe damage, requiring costly repairs or total replacement (Nascimbene 2024). To mitigate this, metallic dampers, which dissipate energy through large plastic deformations, are widely used to enhance the seismic resilience of civil structures by reducing potential damage to the primary gravity-load resisting system (Nascimbene et al. 2025). Braced frame systems, in particular, are widely relied upon for their high lateral stiffness and efficiency. However, their seismic performance is intimately linked to the buckling stability and post-yield behavior of the bracing members, necessitating careful

Extended author information available on the last page of the article

Published online: 07 April 2026

detailing to ensure ductile energy dissipation (Sullivan et al. 2013; Mazzotta et al. 2017; Brunesi and Nascimbene 2025). Consequently, researchers have continuously sought to develop new, more efficient damper designs beyond conventional steel I-sections. Lee et al. (2015) introduced dumbbell-shaped, tapered and hour-glass shaped cutouts in steel plates positioned as shear links (fuses). These dampers provided higher ductility over conventional strip dampers and structural efficiency increased by a factor of 2 ~ 3 times in terms of absorbed energy per unit volume. Zhu et al. (2018) also investigated the performance of optimized shear panel damper subjected to quasi-static cyclic loading and restrained in the out-of-plane direction. The optimized shear-link reached 40%~63% higher energy dissipated compared to the control rectangular shaped link.

Another line of research has focused on butterfly-shaped shear fuses (Farzampour and Eatherton 2019; Esteghamati and Farzampour 2020; Farzampour 2021; Yue et al. 2024; Goshtaei et al. 2024), recognized for aligning their cross-section with typical bending moment distributions. Farzampour (2021) compared the performance of these links to rectangular shaped counterparts, focusing mainly on deriving predictive equations for the critical angle to distinguish between shear and flexure-controlled behavior in these links. Yue et al. (2024) utilized the butterfly-shaped shear fuse as shear keys for small-to-medium span highway bridges, subjected to four different cyclic loading protocols. It was found that the energy dissipation capacity was highly influenced by the loading protocol, while the force-displacement curve was almost unaffected. Hui et al. (2022) introduces a low-cost double-sided slotted steel tube shear. Quasi-static cyclic tests showed stable shuttle-shaped hysteretic curves, strong plastic deformation, and damping coefficients of 0.31–0.40, indicating excellent energy dissipation. Parametric analysis revealed that increasing tube thickness and bending element width enhanced performance, while excessive slot width reduced strength.

To move beyond predefined geometries, topology optimization of structural elements has been widely employed in various fields to improve the performance of structures. Majdak et al. (2024) investigates the energy absorption capacity of two-dimensional (2D) cellular topologies, classified into honeycomb, re-entrant, bioinspired, and chiral groups, under quasi-static compression. Using validated finite-element simulations, the study identifies how geometry and deformation mechanisms influence energy dissipation, with honeycomb-based topologies showing the highest average specific energy absorption. Avecillas and Eatherton (2020) explored other topologies for optimization of shear links using a genetic algorithm-based topology optimization procedure. The study aimed to improve the performance of butterfly-shaped shear links through controlling buckling. The objective function was set depending on both the shear buckling and yield loads. The shear buckling load was determined through 3D eigen-buckling analysis while utilizing 2D plane stress nonlinear analysis. Nguyen and Eatherton (2023a, b) expanded on the optimization of plated shear links, and provided a new design for the links which they label "Tie-butterfly-shaped" link. The idea was to improve the buckling resistance of the butterfly-shaped link, which is already optimized for maximum fracture resistance. Their work involved 4 specimens tested physically, and 69 numerical models. The tied model provided better performance over the straight legs, where ties fractured at 15% to 23% of the shear angle while continuing to resist shear deformation through the undamaged straight parts. Goshtaei et al. (2024) provided a comprehensive study on optimized butterfly-shaped steel plate fuses considering multiple performance metrics (i.e. strength, ductility, and damping). The study offers design

guidelines based on geometric ratios and serves as a tool for enhancing earthquake-resilient structural systems, balancing ductility, strength, and energy dissipation.

Gu et al. (2024) introduced a novel Nonlinear Fatigue, Damage-Constrained Topology Optimization (NFDCTO), which accounts for the nonlinear accumulation of fatigue damage under cyclic loading. Through a series of 2D and 3D benchmark examples, including L-shaped beams, bridge structures, and cantilever beams, the NFDCTO method demonstrated superior reliability and performance over traditional linear fatigue-based approaches. Zhan et al. (2025) proposed a Fatigue Reliability-Based Topology Optimization (FRBTO) framework tailored for compliant mechanisms, considering uncertainties in material properties. Numerical examples demonstrated significant improvements in fatigue reliability compared to deterministic optimization. Monte Carlo simulations validated the robustness of the developed framework, highlighting its potential in engineering applications involving compliant mechanisms under uncertain operating conditions.

The pursuit of innovative geometries continues when Giuliani et al. (2024) experimentally validated the performance of Dissipative Replaceable Link Frames (DRLF) demonstrating that such systems can achieve stable hysteretic behavior, large energy dissipation, and easy post-earthquake replacement, thus substantially improving structural resilience. Similarly, Ebrahimi Majumerd et al. (2023) proposed a base-rocking dual-core braced-frame system equipped with vertical Buckling-Restrained Fuses (BRFs) that effectively prevents soft-story formation and allows interchangeability of energy-dissipating components. Building upon the concept of accessibility and maintenance, Luo et al. (2024) introduced structural access panels that facilitate post-earthquake inspection of hidden dissipative devices, particularly in Eccentrically Braced Frames (EBFs), reducing downtime and inspection costs. Louzai and Abed (2025) developed a simplified design procedure for retrofitting reinforced-concrete frames with eccentric steel braces containing vertical shear link elements, emphasizing the importance of shear-dominated yielding for stable hysteresis and rapid repairability while maintaining computational efficiency. It is worth noting that the design objectives for metallic dampers often involve a trade-off between stiffness and spectral demand. In many retrofit applications, low-stiffness dampers are preferred to dissipate energy without shortening the structural period, thereby avoiding increased spectral acceleration demands. However, in the context of EBFs, the shear link serves as the primary lateral stiffness provider. Consequently, high initial stiffness is often a critical design requirement to satisfy inter-story drift limits under wind and frequent seismic events. The topology-optimized links proposed herein are specifically tailored to maximize this stiffness-to-volume ratio, accepting the potential for higher base shear demands in exchange for superior drift control and stability.

Bustos et al. (2025) investigated octagonal (cellular) shaped shear links acting as passive dampers for energy dissipation. Even though it is not explicitly mentioned in their work, the study paves the way for more research into the adoption of cellular and lattice structures for passive dampers subjected to cyclic loading. Ramonell and Chacon (2021) and Saleh et al. (2024) leveraged the use of topology optimization in 3D spatial domain for optimizing links in eccentrically braced frames (EBF). Ramonell and Chacon (2021) studied both flexural and shear links aligned as horizontal links, while Saleh et al. (2024) focused on vertical shear links. Both studies provided links with superior performance compared to conventional links, however, the only challenge that remains is manufacturing of such complex

shaped links. The resulted topology of the optimized link in (2024) had an X-shape, which is somewhat similar to the approach that Guo et al. (2020) studied in their work.

To address the manufacturing challenges inherent in complex geometries, Saleh et al. (2024) suggested using wire and arc additive manufacturing (WAAM) to produce topology-optimized shear links. WAAM excels in fabricating larger, thicker steel sections but can introduce issues like residual stresses, distortions, or porosities. Accordingly, this incentivizes more research on new optimized shear links topologies if additive manufacturing will be used to manufacture these parts. Laghi et al. (2025) investigated the tensile strength of WAAM fabricated steel bars using dot-by-dot technique. The study includes the influence of build angles (0°, 10° and 45°) on the tensile properties, as illustrated in Fig. 1. Other researchers also attempted to manufacture grid shaped steel and aluminum (Abe and Sasahara 2019; Yu et al. 2021, 2022; Li et al. 2020; Liu et al. 2023; Zhang et al. 2020; Khosravani et al. 2025; Xu et al. 2024).

Another interesting approach that does not require extensive material deposition using WAAM is strengthening of conventional steel sections by adding material strategically to improve strength and stiffness. Baqershahi et al. (2024) demonstrated that a hybrid manufacturing approach, which combines WAAM and conventional manufacturing (CM), can reduce environmental impact compared to CM-only beams. Yang et al. (2025) leveraged WAAM to increase the ultimate bending resistance of steel I-sections by 11.5% to 33.2%, also the increase in initial stiffness reached 35.9% with very limited increase in masses (2.6%~12.3%). Kloft et al. (2023) and Gardner et al. (2024) also introduced strengthening of IPE sections using WAAM. These approaches of hybrid manufacturing, where both subtractive and additive manufacturing are used for the final part, can be environmentally beneficial (Baqershahi et al. 2024).

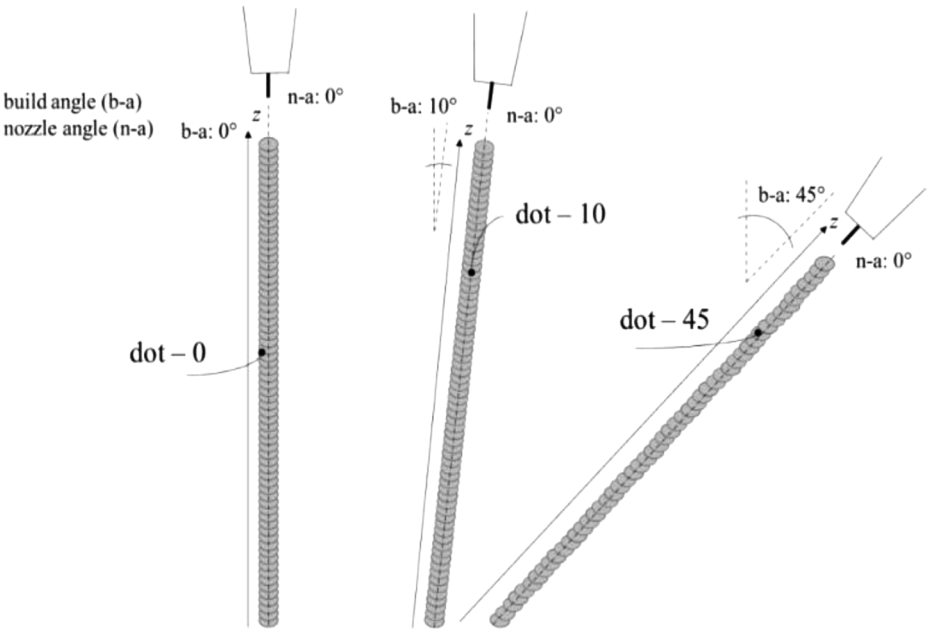

Fig. 1 Dot-by-dot WAAM of steel bars adopted from (Laghi et al. 2022)

The primary objective of this study is to bridge the gap between theoretical topology optimization and practical seismic application in Eccentrically Braced Frames (EBFs). While previous research has demonstrated the theoretical potential of topology-optimized (TO) shear links, widespread adoption has been hindered by manufacturing complexities and the susceptibility of complex geometries to premature ductile fracture. This study advances the state of the art by shifting the focus from pure topology optimization to manufacturable hybrid design. The specific novelty of this work is threefold: (1) the introduction of hybrid manufacturability and stiffening strategies for TO links; (2) the implementation of a fracture-aware numerical framework, ensuring that new geometries actively mitigate stress concentrations rather than solely maximizing stiffness; and (3) a system-level performance investigation where stiffened TO links are assessed within full-scale EBF frames to quantify the trade-offs between component stiffening and global frame ductility. To achieve these objectives, the study adopts a multi-stage numerical framework utilizing the ABAQUS. First, the sensitivity-based Solid Isotropic Material with Penalization (SIMP) method is employed to generate the baseline topology-optimized geometry under linear-elastic conditions. Second, a parametric design phase introduces stiffening elements and braces to the optimized backbone, simulating a hybrid manufacturing approach. Third, the seismic performance of these designs is evaluated through non-linear finite element analysis incorporating damage initiation and evolution criteria. While other parametric optimization algorithms such as Non-dominated Sorting Genetic Algorithm (NSGA-II) or Artificial Bee Colony (ABC), have been successfully applied to optimize the sizing and shape parameters of known geometries, continuum topology optimization methods, such as the (SIMP) approach, allow for free-form material distribution within a design domain. Consequently, this study adopts the SIMP method followed by a parametric study to integrate stiffeners and braces for manufacturing and buckling resistance. The strength, stiffness and energy dissipation capacities are assessed and compared against conventional shear link. The outcomes underscore the feasibility and advantages of leveraging WAAM to improve the performance of shear links for seismic applications.

2 Topology optimization of shear links

The shear-link topology optimization was performed with the sensitivity-based density method implemented in the Abaqus Topology Optimization Module (ATOM). Following standard practice for stiffness design, the problem was posed as a minimum-compliance formulation under a prescribed linear-elastic load case. The finite-element equilibrium for a given material distribution $\rho = \{\rho_e\}_{e=1}^{N}$is:

$$K(\rho)U = F \tag{1}$$

Where U is the global displacement vector, F the applied load vector, and K(ρ) the assembled stiffness matrix. The objective (compliance) equals the total strain energy provided in the following equation:

$$\min_{u,E_e} : c = U^T K U = \sum_{e=1}^{N} u_e^T k_0(E_e) u_e \tag{2}$$

Where u_e is the displacement vector for individual element (e = 1,2,3 … . N), k is the stiffness matrix for element "e", which is a function of Young's modulus for an element with intermediate density, described in (Eq. 3):

$$E = \rho^P E_0 \tag{3}$$

Where ρ is the element relative density factor, p is the penalty factor that defines the effect of the density on the model stiffness, and E_0 is the Young's modulus of the fully solid material. Material stiffness is modeled using the SIMP (Solid Isotropic Material with Penalization) scheme with a penalty factor of 3 to interpolate the material stiffness, following the standard practice in topology optimization literature for structural applications (Bendsoe and Sigmund 2013). This value provides a good compromise between driving the design toward discrete material distribution and maintaining numerical stability and convergence. Using a lower penalty value, such as 2, typically leads to excessive intermediate densities and less clear structural boundaries, while higher values, such as 4 or above, tend to introduce mesh dependency and convergence issues due to the steep nonlinearity of stiffness-density interpolation (Sigmund and Maute 2013). Therefore, a value of 3 is widely adopted to yield manufacturable, binary-like designs with stable optimization behavior (Bendsøe and Sigmund 1999). The convergence criteria were set such that the relative delta objective function (volume change) between consecutive iterations dropped below 0.1%.

The design domain is a solid rectangular beam constrained to the same volume of the original Reference Shear Link (RSL-1) provided by Liu et al. (2017), ensuring the optimized shape maximizes stiffness while preserving or slightly reducing the material volume. It is acknowledged that the minimum-compliance formulation assumes linear-elastic behavior, whereas shear links are designed to undergo significant inelastic deformation and energy dissipation during seismic events. In this study, constraints regarding buckling stability, local stress concentrations, and manufacturability were not explicitly imposed within the ATOM optimization algorithm. Instead, these performance criteria were addressed in a post-optimization design phase. The raw topology-optimized geometry (TO-00) served as a baseline backbone, which was subsequently refined and stiffened (Models TO-P1 through TO-B2) to prevent premature buckling and facilitate hybrid manufacturing (CNC + WAAM), as detailed in Table 3.

The optimization process converged at the 25th iteration. The TO link was subsequently tested within an eccentrically braced frame setup and compared with conventional vertical links provided by Lian and Su (2017). The full optimization workflow and resulting topology optimized link are provided in Fig. 2.

The proposed TO link proved to have higher stiffness and strength, resulting in higher energy dissipation. Figure 3(a) provides the shear deformation of RSL-1 due to lateral displacement, which can be expressed as compression on one diagonal and tension on the other. Figure 3(b) provides the vectors for the resulting principal stresses from the shear deformation of the optimized links obtained from the FE analysis. It can be observed that the load-bearing mechanism shifts from conventional shear action to a tension-compression behavior resembling a strut-and-tie model. This internal force redistribution enhances both the strength and stiffness of the links.

Nevertheless, high stress concentration at the connection with end plates, redundancy and the manufacturability of the part still warrant further investigation. In order to reach the

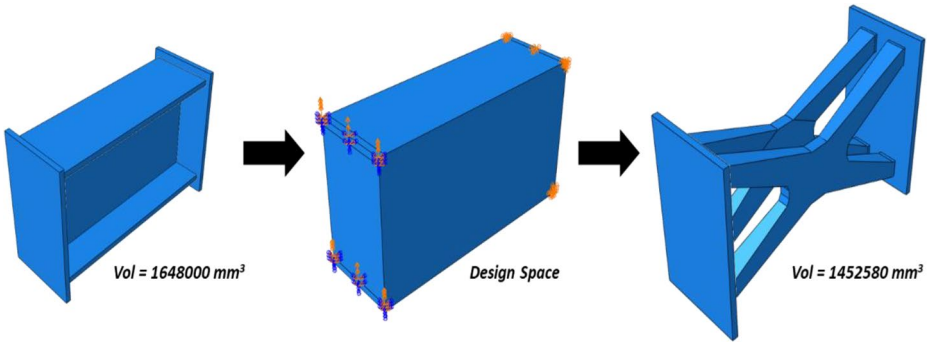

Fig. 2 TO workflow and final optimized link (Saleh et al. 2024)

full capacity of the link, it is crucial to have high quality welds with the end plates to avoid premature failure. Consequently, this paper provides high fidelity numerical investigation of conventional and TO links considering damage and fracture in the models and proposes new designs for the TO link. The study investigates topology optimized links while considering the damage that might occur to the link that can lead to pre-mature failure. Afterwards, the behavior of the proposed new designs are then investigated individually and in eccentrically braced frames (EBF) setup, taking into consideration the aforementioned challenges.

3 Numerical analysis

Since the work presented is mainly dependent on numerical analysis, it is essential to capture the damage and fracture that took place in the validation models. Afterwards, the validated constitutive models are adopted for the proposed TO links.

3.1 Modelling fracture and damage

The accurate prediction of ductile fracture in structural steels under cyclic and complex loading is essential for reliable performance-based design and assessment of structural components such as beams and shear links. Ductile fracture in metals is typically governed by void nucleation, growth, and coalescence processes, which are strongly influenced by stress triaxiality (η), and plastic strain localization. Among the most widely used models are the Stress Modified Critical Strain (SMCS) model (Hancock and Mackenzie 1976) and the Void Growth Model (VGM) (Rice and Tracey 1969), both of which are micromechanics-inspired and have been successfully applied to Q345 steel. The SMCS model establishes a critical fracture strain that is exponentially dependent on stress triaxiality (η). This model has been implemented in several studies due to its relatively simple form and ease of calibration. Liao et al. (2011) calibrated the SMCS model for Q345 steel through monotonic tensile tests on base metal, deposited metal, and heat-affected zones, demonstrating its capacity to accurately predict fracture initiation in welded steel connections. The model assumes fracture occurs when the following condition is met:

$$\varepsilon_f = \varepsilon_0 . exp\left(-\alpha . \eta\right) \tag{4}$$

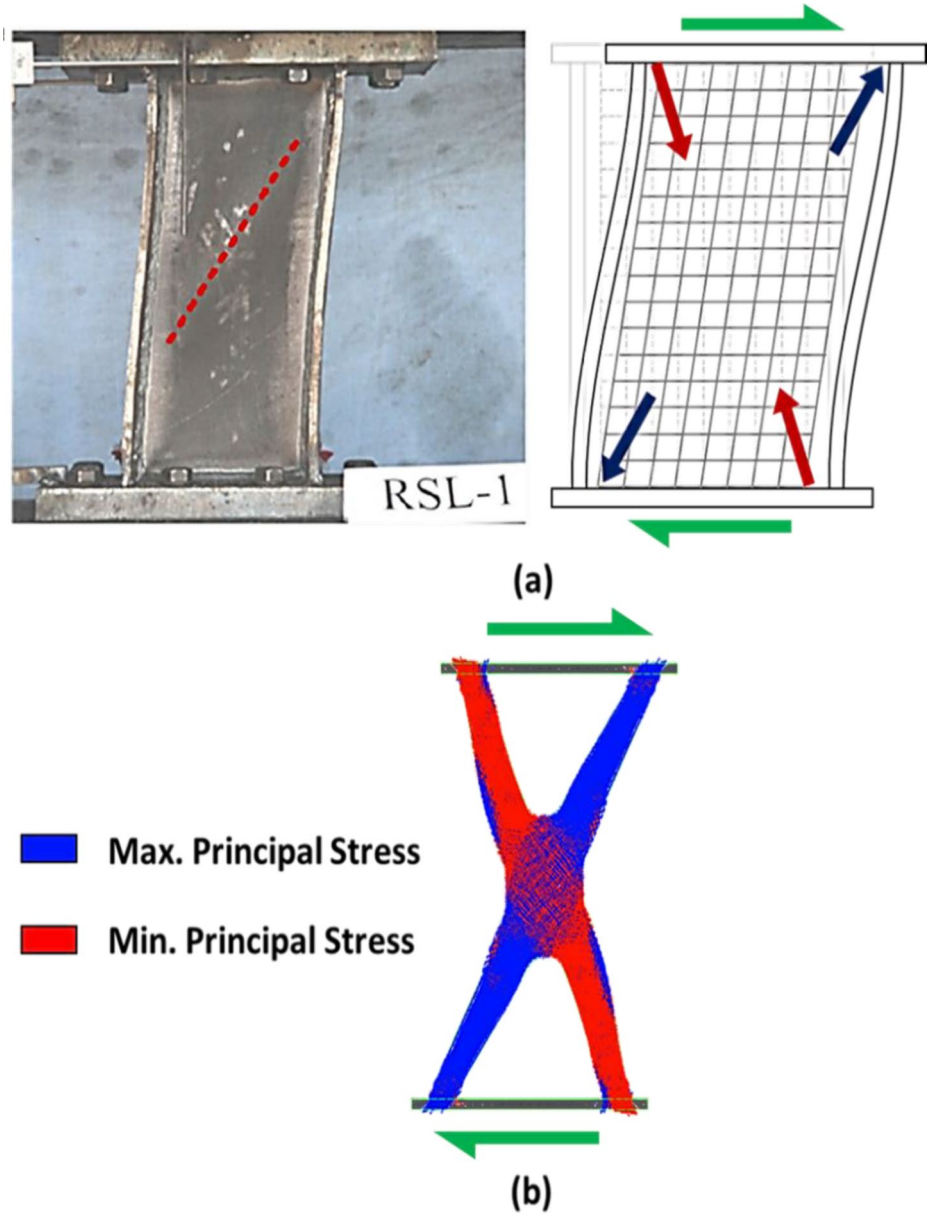

Fig. 3 Shear deformation in (**a**) conventional link versus the principal stresses' vectors obtained from the FE analysis of (**b**) optimized link

where ε_f is the equivalent plastic strain at fracture, ε_0 is a material constant, and α reflects the sensitivity to triaxiality (Liao et al. 2011). Similarly, the VGM is based on the exponential growth of a spherical void under hydrostatic stress. The VGM integrates the effects of stress triaxiality and plastic strain over time to predict failure initiation. It has been shown to cor-

relate well with observed fracture behavior in steel connections under monotonic loading (Liao et al. 2011; Kanvinde and Deierlein 2006).

Experimental calibration studies specifically targeting Q345 steel were carried out by Li et al. (2020), who proposed a modified Coffin-Manson model incorporating stress triaxiality as a governing parameter. Additionally, a more relevant study was conducted by Xie et al. (2025). Their work expanded on this by examining ultra-low-cycle fatigue (ULCF) in Q345 steel under combined tension-shear for estimating the energy dissipation capacity of shear metallic dampers (shear links). They developed the cyclic shear-void damage model (CSVDM), which introduces a damage locus based on both stress triaxiality and Lode angle to capture shear-induced failure. The results confirmed that failure prediction is significantly improved when both stress state and loading history are accounted for. Fig. 4 provides stress triaxiality (η) versus the experimental fracture strain for Q345 steel that is used in the current study and adopted from the work of Xie et al. (2025).

While the adopted CSVDM framework improves upon traditional models by incorporating Lode angle sensitivity for shear-dominated stress states, explicit limitations regarding multiaxial cyclic loading remain. The model assumes a phenomenological approach to damage accumulation, utilizing a stress triaxiality cut-off to simulate the arrest of void growth under compressive stress states. This simplification does not fully capture micromechanical phenomena such as void flattening, shape distortion, or the partial healing effects observed under complex non-proportional loading paths. Consequently, while the model is calibrated to capture the macroscopic fracture initiation point for Q345 steel, it serves as a continuum-level approximation of the underlying microstructural degradation.

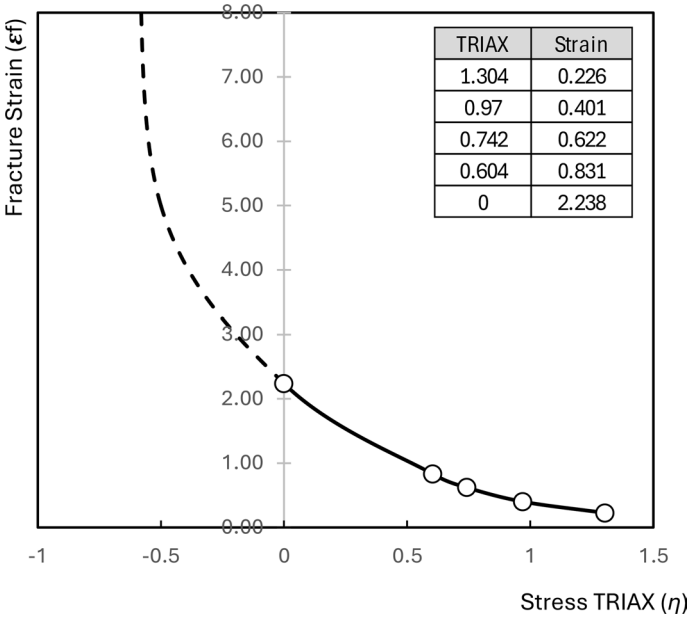

Fig. 4 Stress triaxiality versus fracture strain relationship for Q345 steel (Xie et al. 2025)

3.2 FE analysis and verification of shear link (RSL)

The numerical analysis presented herein builds upon the experimental program of Liu et al. (2017). In their work they studied shear links with a fixed length (400 mm) while varying cross-sectional properties and stiffener locations. Their work is adopted here due to the thorough characterization of Q345GJ steel's cyclic behavior, which demonstrated strong low-cycle fatigue capacity ideal for shear links in seismic applications, while the materials properties are provided in Table 1. RSL-1's flange dimensions were 130 mm width and 10 mm thick. The total depth of RSL-1 was 210 mm, having an 8 mm web with no stiffeners. Distributed plasticity was explicitly simulated using 8-node linear brick elements (C3D8R) with reduced integration for the link's flanges and web, having a mesh size not exceeding 5x5x5 mm. This element formulation was selected to eliminate shear and membrane locking phenomena often observed in fully integrated elements subjected to bending. Furthermore, the enhanced hourglass control associated with this formulation effectively minimizes spurious zero-energy modes, ensuring numerical stability during large plastic deformations (Nascimbene 2013). To account for second-order effects and significant shape changes during the loading protocol, geometric nonlinearities were incorporated into the analysis. The link's flanges are welded to the endplates using double bevel full-penetration groove weld, while fillet welds were used to connect the web to the flanges and the endplates. Consequently, the fillet welds are modelled using C3D8R elements, however, tie constraints between the flanges' ends and the endplates are sufficient to represent the full-penetration groove weld. The interaction between the welds and base metal plates are modeled using surface-to-surface interactions with cohesion properties having shear and normal strengths equal to that of the base metal. The material model used for the numerical analysis of individual shear links adopts the one presented by Liu et al. (2017) and presented in Table 1 which summarizes the constitutive model parameters, including isotropic and kinematic hardening properties. The link is fixed at one end, while lateral displacement is applied to the other end, following the loading protocol of AISC341-16.

The deformed shapes are provided in Fig. 5, showing the von-mises and shear stresses on the links. It can be noticed that the failure mode includes separation of the web from the flanges at the location of the welds, which goes in accordance with the failure mode observed in the experimental program. Moreover, the load-displacement (force-drift) curves provided in Fig. 6 show that the numerical model is in very close agreement with the tested RSL-1.

3.3 FE analysis and verification of EBF

A numerical model for the EBF was developed and validated against the experimental setup reported by Lian and Su (2017). The material properties for the different structural elements of the EBF are presented in Table 2. To enhance the accuracy of the simulation, material damage was incorporated into the numerical model, resulting in a closer agreement with the experimental results compared to the study by Saleh et al. (2024). The adopted damage

Table 1 Q345GJ material properties (Liu et al. 2017)

Parameter	$\sigma^o\,(MPa)$	$C_1\,(MPa)$	γ_1	$C_2\,(MPa)$	γ_2	$C_3\,(MPa)$	γ_3	$C_4\,(MPa)$	γ_4
Q345GJ	350	20 000	1000	10 000	100	600	20	350	10

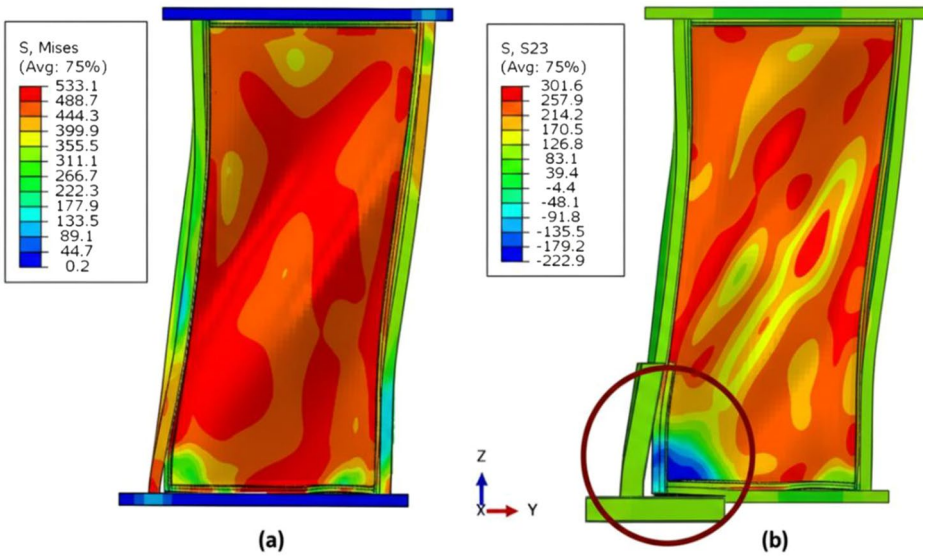

Fig. 5 Deformed shapes of RSL-1 numerical models showing (**a**)Von-mises and (**b**) shear stresses on the link

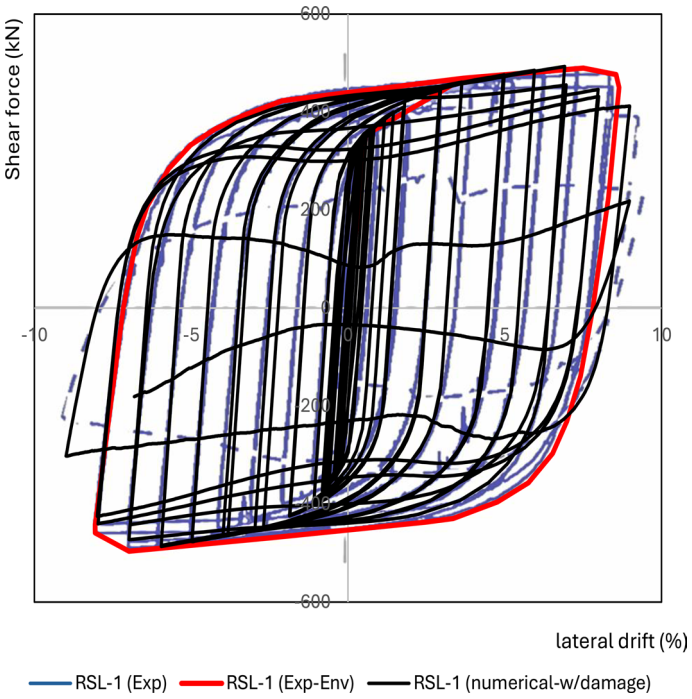

Fig. 6 Hysteresis loops from the numerical model vs. experimental program (Liu et al. 2017)

Table 2 Material properties for EBF structural members (Lian and Su 2017)

Structural member	Links	Braces	Beams	Columns
Steel grade designation	**Q345**	**Q460**	**Q460**	**Q460**
f_y web (MPa)	427.4	496.9	496.9	496.9
f_y flange (MPa)	383.33	468.77	468.77	468.77
f_u web (MPa)	571.1	658.57	658.57	658.57
f_u flange (MPa)	554.4	627.97	627.97	627.97
Web elongation %	26.53	29.73	29.73	29.73
Flange elongation %	31.01	35.88	35.88	35.88

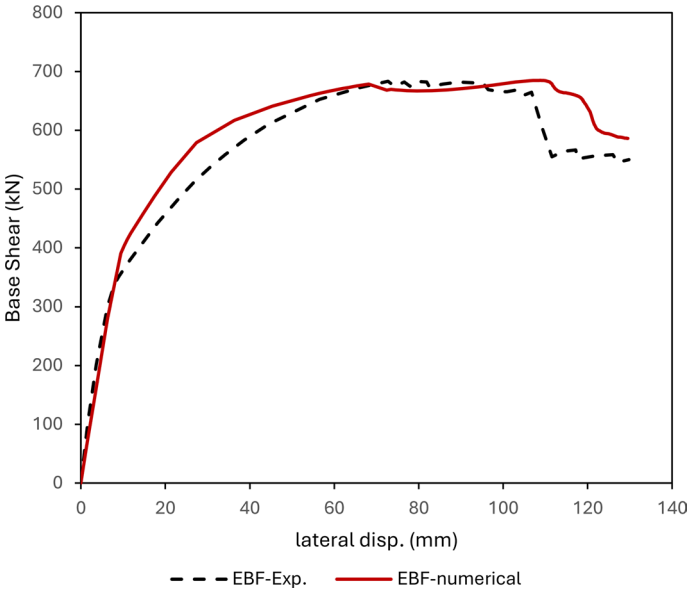

Fig. 7 Results of experimental (Lian and Su 2017) vs. numerical model of one-storey EBF system

model was based on the work of Xie et al. (2025) on Q345 steel, which was the steel grade used for vertical shear links. Fig. 7 provides the comparison between the experimental and numerical base shear–lateral displacement responses.

3.4 TO models' description

The initial proposal for fabrication of the original TO shear link proposed using WAAM technology due to the irregularity of the shape. Alternatively, a different hybrid approach is proposed herein, where most of the link would be fabricated using conventional subtractive cutting of steel plates using computer numerical control (CNC), while using WAAM – if necessary - to strengthen the link. Table 3 provides a summary of the proposed links in this paper.

TO-00 represents the original optimized link, and as described in Table 1-a, it is proposed that an 18-mm 2D plate be cut in the desired X-shape and then use WAAM to finalize the required optimized geometry. Figure 8 presents the dimensions of the TO-links. The TO-00 link followed the dimensions labeled as Model (x), whereas all other links adopted the

Table 3 Proposed adjustments on TO shear links with similar final mass

CNC WAAM		
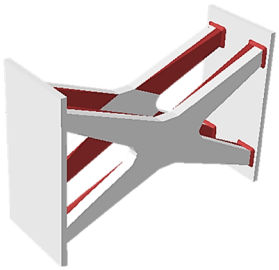 (a)	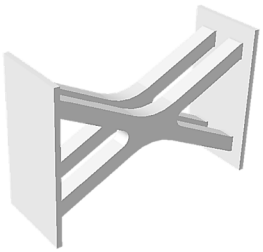 (b)	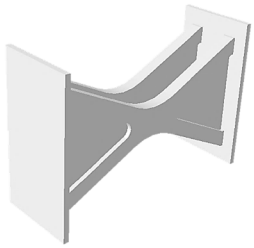 (c)
Original TO-Link **Label**: TO-00 **Description**: 18mm X-plate strengthened with WAAM	**Label**: TO-01 **Description**: 32mm X-plate without strengthening	**Label**: TO-P1 **Description**: 26mm X-plate strengthened with 6mm plates
 (d)	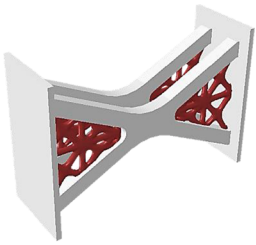 (e)	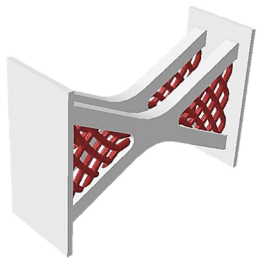 (f)
Label: TO-P2 **Description**: 24mm X-plate strengthened with 8mm plates	**Label**: TO-B1 **Description**: 26mm X-plate strengthened with 2x2 x-shaped braces.	**Label**: TO-B2 **Description**: 26mm X-plate strengthened with 4x4 x-shaped braces.

dimensions of Model (y). This selection was based on an extensive parametric study conducted on all the proposed configurations. TO-01 assumes a constant thickness of approximately 32 mm for the X-shaped plate to get the same volume of the optimized link, with no tapering in any direction. Stiffeners of 6 mm thickness are added to the X-plates in TO-P1, while thicker stiffeners are used for TO-P2 to test the effect of changing the thickness of stiffeners on the strength and ductility of the links. The final shape for TO-P1/P2 can also resemble the butterfly-shaped links from literature. In TO-B1, instead of using plates, truss shaped 2×2 X-braces with 10 mm diameter are added to stiffen the link, while in TO-B2, 4×4 8 mm diameter braces are used. The proposed designs for TO-B1 and TO-B2 are also based on a parametric study that was built on studying the behavior of TO-P1/P2 which

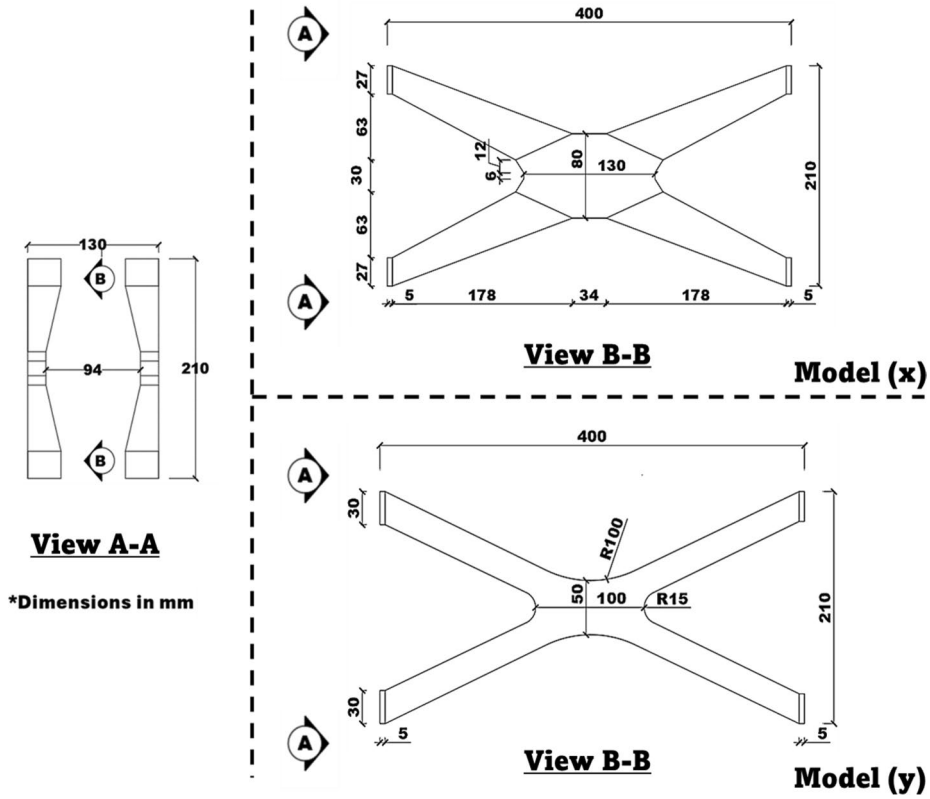

Fig. 8 Dimensions for the TO links' plates. Model (**x**) is used for TO-00 while model (**y**) is used for all the other TO links

showed promising results compared to both the conventional and original TO links. Figure 9(a) shows the vectors for the resulting principal stresses from the shear deformation of the TO-P1/P2 links. Consequently, it was hypothesized that if the stiffening plates are to be replaced with truss shaped stiffeners having the same final volume, the performance of the links can be improved. Figure 9(e) shows different designs that were part of the investigation, while Figs. 9(b) and 9(c) resembles TO-B1 and TO-B2 respectively. It is essential to note that all proposed links have the same masses of the original link with variation less than −1% compared to TO-00 and the proposed plates' thickness in any of the designs considered only this aspect. The patterns for TO-B1 and TO-B2 are inspired by the projection of body-centered cubic (BCC) and dodecahedral lattices on 2D planes known for energy dissipation. It is also worth mentioning that WAAM-produced steel parts manufactured from carbon steel have shown to have limited anisotropic behavior, unlike that of austenitic stainless steel (Wang et al. 2024; Huang et al. 2022; Kyvelou et al. 2020). Accordingly, the material constitutive model for the WAAM parts is modeled as isotropic with properties identical to the base metal. It is acknowledged that this is a numerical idealization. In physical applications, WAAM processes can introduce direction-dependent anisotropy, residual stresses due to thermal cycles, and geometric imperfections such as surface roughness or porosity. While literature indicates that carbon steel exhibits limited anisotropy compared to stainless steel,

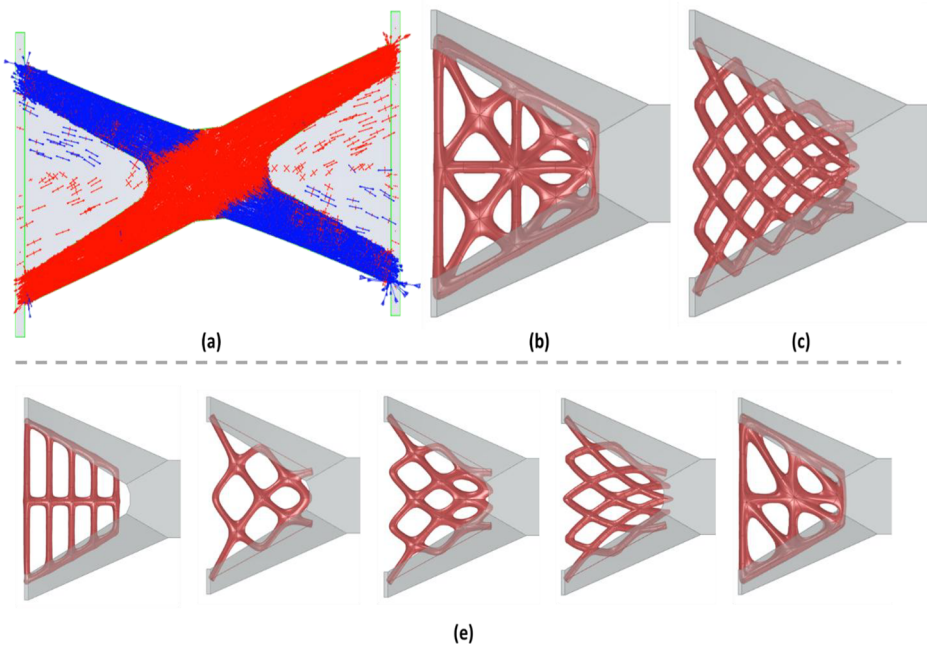

Fig. 9 (**a**) Principal stresses' vectors in TO-P1/P2 against proposed stiffening approaches (**b**) TO-B1, (**c**) TO-B2, and (**e**) other stiffening trials

these manufacturing defects could locally accelerate damage initiation or reduce low-cycle fatigue life. However, the proposed hybrid manufacturing strategy mitigates these risks by relying on the CNC-cut rolled plate for the primary load path, utilizing WAAM primarily for stiffening elements where such imperfections have a reduced impact on global stability.

3.5 Optimized shear links

ABAQUS static (general) implicit solver was used for the analysis. 8-node linear brick elements with reduced integration (C3D8R) were used to model all links, with mesh size not exceeding 5x5x5 mm. The material model of the links was updated to include damage initiation and evolution. The damage simulation in ABAQUS tracks the cumulative accumulation of equivalent plastic strain at every time increment. The damage initiation criterion is evaluated continuously throughout the cyclic history, rather than solely at peak displacement amplitudes. Once the criterion is satisfied (damage initiation variable ≥ 1.0), the material stiffness degrades according to the damage evolution law based on fracture energy. This allows the model to capture the progressive deterioration of the steel during the hysteresis loops. To assess the performance of the links, a monotonic displacement was applied once to each link and displacement-controlled cyclic load, corresponding to the standard load case provided by (Liu et al. 2017), was applied as well. Fig. 10 provides the load-displacement curves for all six links in addition to the original RSL-1, while Fig. 11 summarizes the maximum recorded shear force for each link from the monotonic load case.

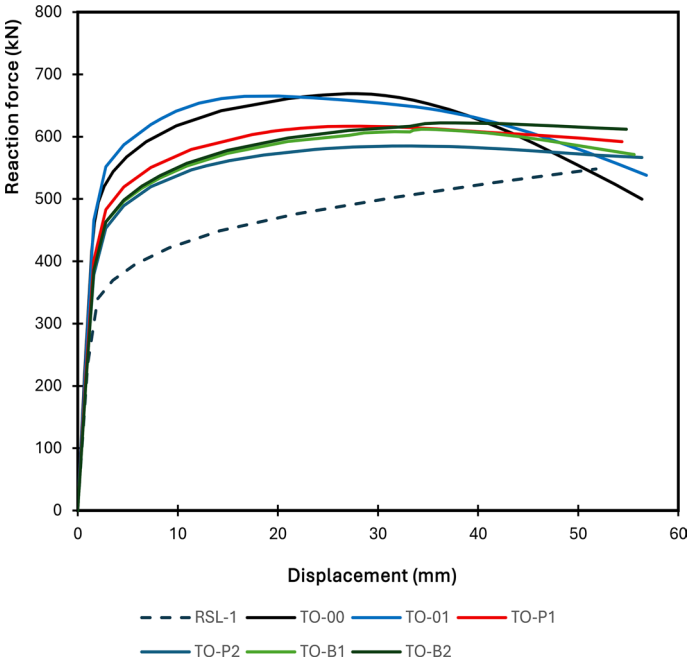

Fig. 10 Load-displacement curves for optimized links

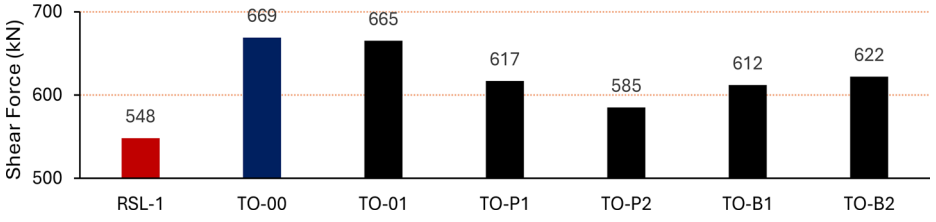

Fig. 11 Maximum shear forces recorded for the links (monotonic load)

The initial elastic stiffness appears similar across all TO-links, slightly higher than RSL-1. TO-00 provided the highest shear force of 669 kN but only 0.5% higher than TO-01, (7–7.5%) higher than TO-P1, TO-B1 and TO-B2, and 12.5% higher than TO-P2. Aside from TO-00 and TO-01, all other links showed a relatively stable post-peak behavior. Moreover, TO-01 was the first to reach its full capacity at approximately 17 mm displacement. TO-P2 showed the least strength while TO-00 showed the least ductility. In terms of monotonic loading, the load-displacement curve for TO-P2 shows that using planar, stiffened butterfly-shaped links resulted in the least promising results compared to the conventional I-section (RSL-1). Additionally, when comparing TO-P1 and TO-P2, it can be noticed that using stiffeners of thickness 6-mm (TO-P1) provided better strength over the 8-mm model.

The links are then subjected to cyclic loading as explained earlier. Figure 12 provides the damage initiation in the links after the 26th cycle which corresponds to a displacement amplitude of 36 mm. The damage initiation provides a scale of the damage percentage that

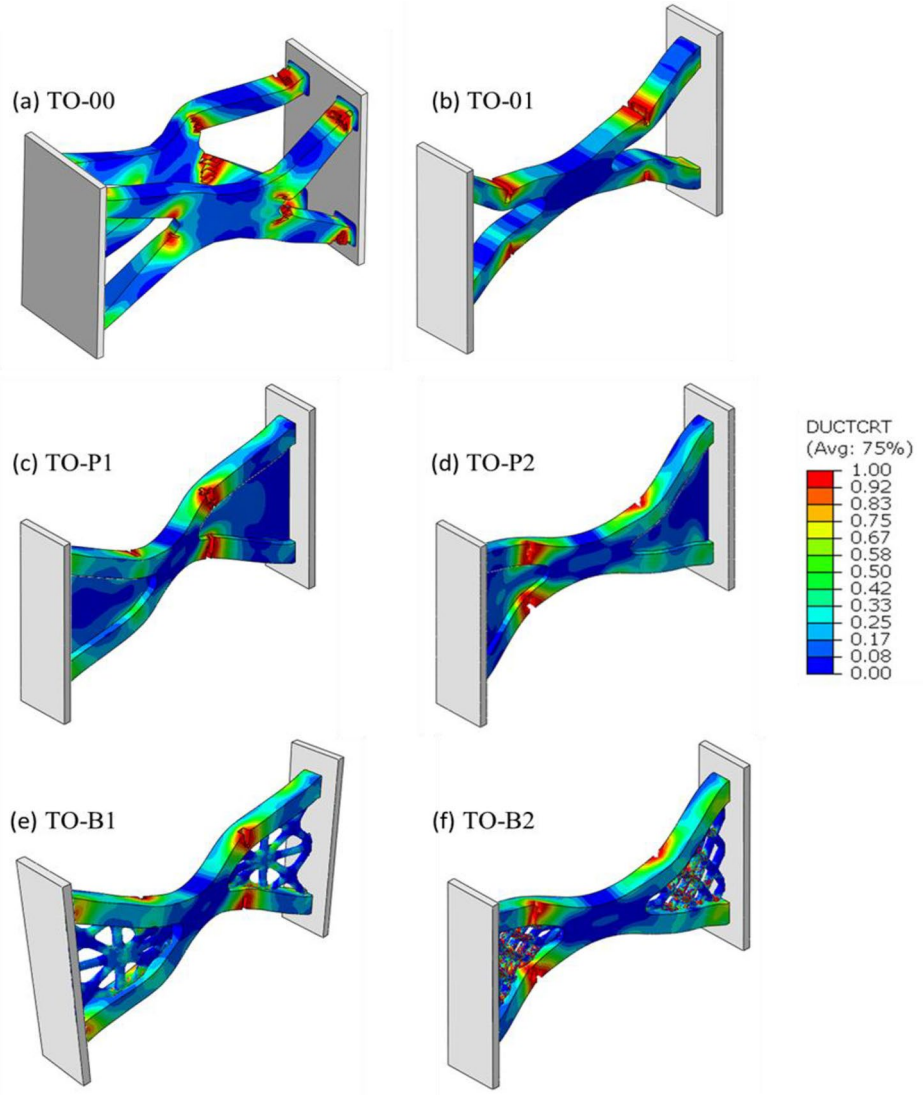

Fig. 12 Damage initiation for the TO-links subjected to cyclic displacement at Δ=36 mm (26th cycle)

took place at the links, ranging from 0 (no damage), to 1 (damaged elements). Figure 13 provides the Von-mises stresses at the end of the 26th cycle as well. It can be noticed that TO-00 was the only link to exhibit damage both at the intersection of the legs with the end-plates and at the intersection of the legs with the center of the link. The other TO links were damaged almost at the center of the legs. Figures 14 and Fig. 15 illustrate the hysteresis load-displacement curves, while Fig. 16 shows the cyclic envelope for all links. The damage observed in TO-00 is translated into a steep drop in strength as shown in Fig. 16, while the other links showed a gradual decrease in strength compared to TO-00. By the end of the 26th cycle, TO-B2 and TO-B1 had the highest residual strength, respectively. They could also

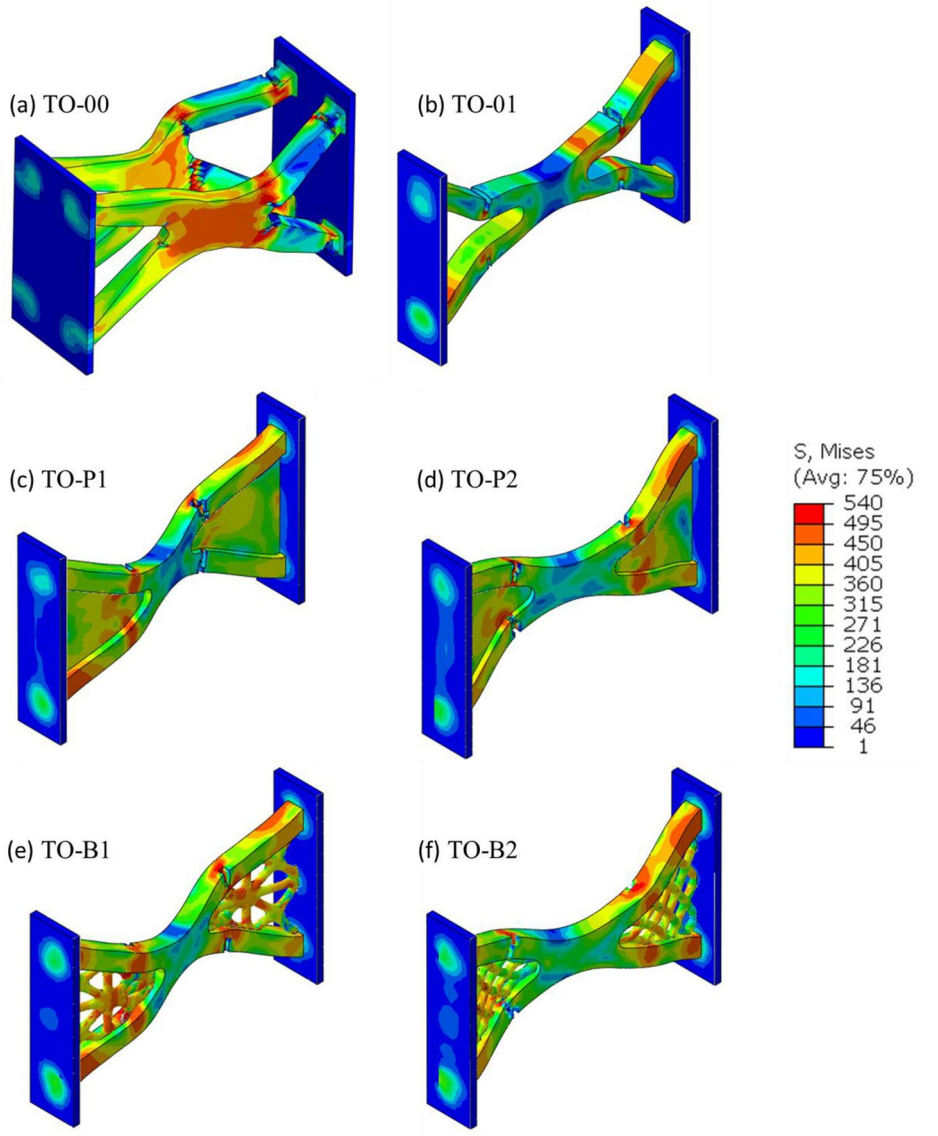

Fig. 13 Von-mises stresses and deformed shape for TO-links subjected to cyclic displacement at Δ=36 mm (26th cycle)

withstand more cycles beyond the 26th, but due to numerical non-convergence in other links beyond the 26th cycle as result of severe damage, the output reported here compared the performance below the 36 mm displacement threshold. This instability arose from severe damage accumulation and subsequent element deletion (fracture) in the critical regions, effectively signifying the complete structural failure of the link.

The variance in post-peak behavior among the link typologies can be attributed to the distinct stress states induced by the stiffening strategies. For the baseline TO-00, the abrupt

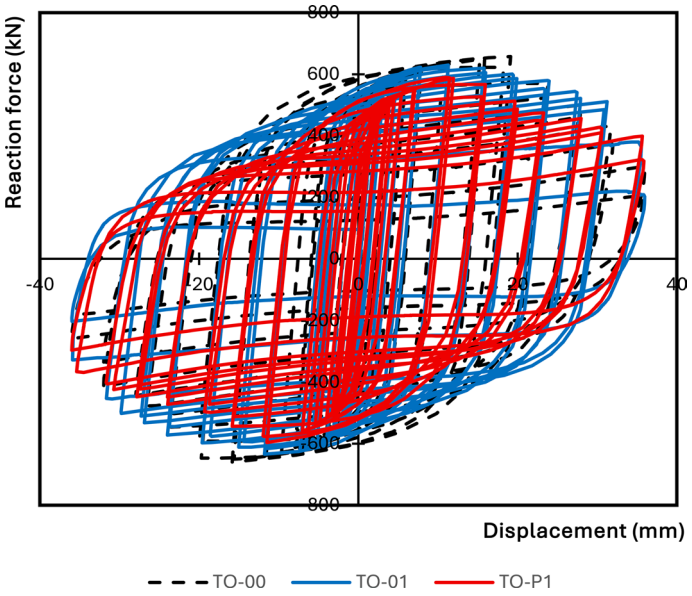

Fig. 14 Load-displacement curves for cyclic loading of links TO-00/01/P1

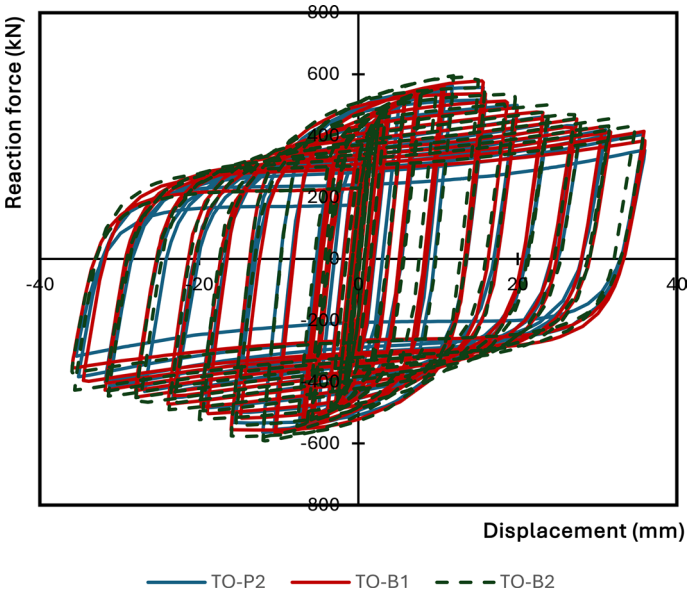

Fig. 15 Load-displacement curves for cyclic loading of links TO-P2/B1/B2

loss of strength (Fig. 18) is driven by severe stress concentrations at the re-entrant corners where the X-legs meet the endplates. This geometric discontinuity creates a region of high stress triaxiality, which, according to the SMCS/CSVDM criterion, accelerates void nucleation and growth, leading to rapid crack propagation and premature failure. In con-

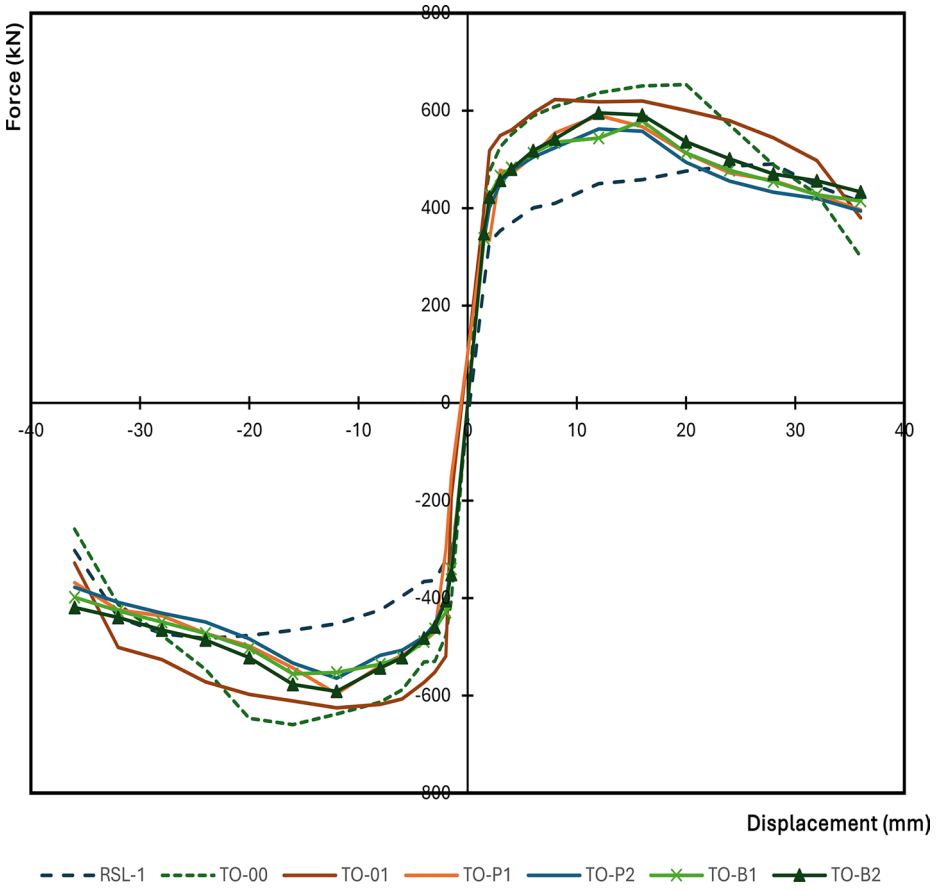

Fig. 16 Cyclic envelope of all optimized links + RSL-1

trast, the TO-P variants utilize stiffeners that function effectively as flanges, increasing the local moment of inertia and reducing the triaxiality demand at the critical connections. This delays fracture initiation and forces a more distributed yielding mechanism along the link length. Furthermore, the TO-B (truss-stiffened) variants benefit from structural redundancy. The lattice braces provide alternative load paths; as damage initiates in the primary X-plate, the stresses are redistributed to the undamaged bracing elements. This redundancy prevents the sudden localized failure seen in TO-00, resulting in a more stable, gradual degradation of strength and significantly improved global ductility.

In terms of maximum shear force recorded during loading, TO-00 had the highest resistance, but only 4% higher than TO-01 and 10% higher than TO-P1 and TO-B2. TO-P2 had the lowest resistance to shear but was still 14% higher than the conventional RSL-1 link. Figure 17 provides a visual comparison of maximum shear forces. The dissipative capacities of the links are assessed using two approaches: the area under the cyclic envelope curve and the equivalent viscous damping coefficient. It was found that the conventional RSL-1 had the lowest energy dissipation calculated from the cyclic envelope, consistent with its relatively weak shear strength. TO-00 and TO-01 were the highest in that respect, while

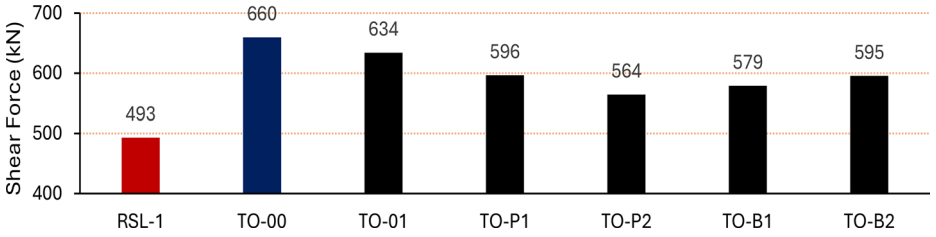

Fig. 17 Maximum shear force recorded during cyclic loading of the links

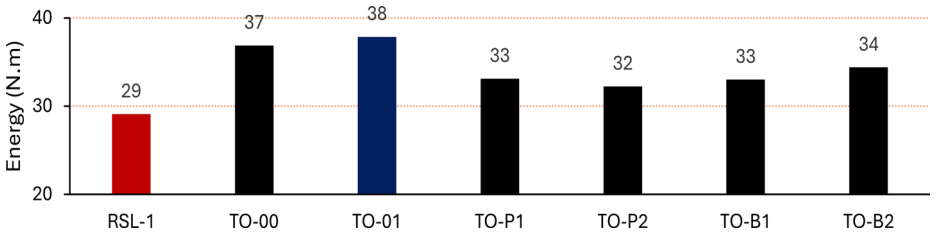

Fig. 18 Energy dissipation comparisons calculated from area under the cyclic envelope curve

TO-P2, which was the lowest, was 10% behind. Figure 18 provides a summary of the calculated energy dissipation in Joules (N.m).

The equivalent viscous damping coefficient is defined using the following equation:

$$\varepsilon_{eq} = \frac{1}{2\pi} \cdot \frac{S_{ABC}+S_{ADC}}{S_{BOE}+S_{DOF}} \tag{5}$$

The terms $S_{ABC}, S_{ADC}, S_{BOE}$ and S_{DOF} are illustrated in Fig. 19 (Wijesundara et al. 2011). S_{ABC} and S_{ADC} resemble the area inscribed (energy dissipated) during one cycle. On the other hand, S_{BOE} and S_{DOF} resemble the total strain energy assuming a linear elastic behavior to the target displacement. Accordingly, $S_{ABC}, S_{ADC}, S_{BOE}$ and S_{DOF} are calculated for all cycles and provided in Fig. 20.

It is important to note that the energy dissipation mechanism of metallic dampers is primarily hysteretic, depending on displacement amplitude rather than loading frequency (velocity). However, to facilitate the use of these links in standard dynamic analyses—such as response spectrum or linear time-history methods—it is common practice to convert this hysteretic energy into an equivalent viscous damping representation. This allows the nonlinear dissipative behavior to be approximated as a linear viscous damping ratio within the structural model.

All links showed comparable damping coefficient, with RSL-1 being the highest but with a small margin. TO-P1 and TO-P2 recorded the lowest damping coefficients, but only 4% behind RSL-1. In conclusion, as a final assessment considering all the mentioned parameters from the monotonic and cyclic load cases, it can be argued that the TO links provided better performance compared to the conventional link. To further assess their structural behavior in a realistic context, the optimized links were subsequently implemented within a single-story EBF system for integrated system-level analysis.

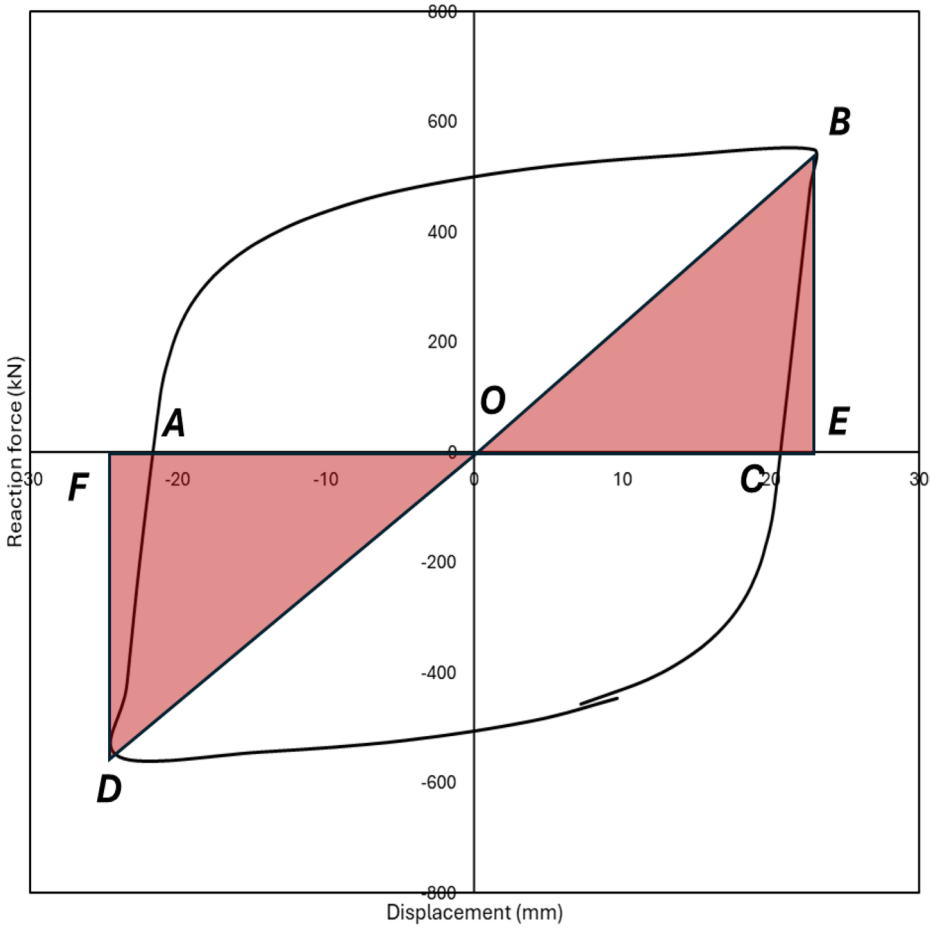

Fig. 19 Hysteretic area for equivalent viscous damping calculation

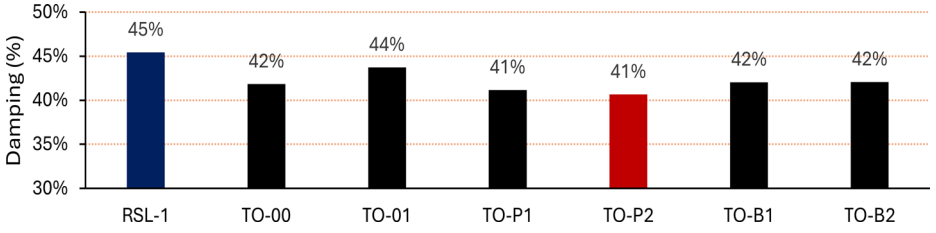

Fig. 20 Equivalent viscous damping coefficient for all links

3.6 Links in EBF

The different optimized links discussed in Sect. 3.5 are tested (numerically) in EBF systems. The setup is adopted from Lian and Su (2017) and validated numerically, as shown in Fig. 7, under monotonic lateral load. The conventional shear link had different web and flange material properties as described in Table 2, therefore, the optimized links were once modeled using the web material model and once using the flange material model. The naming conventions follow the same sequence described in Table 3, for instance, EBF-00-W refers to the original TO link while using web material model, and EBF-00-F refers to the same link using flange material model. The EBF, along with the tested links, are provided in Fig. 21. It is worth noting that the component-level results demonstrated that TO-B2 did not offer significant performance advantages over TO-B1, hence, the TO-B2 model was excluded from the EBF system analysis.

All models were subjected to monotonic displacement to test the strength and stiffness of the EBF system. Figure 22 provides the base shear versus the lateral displacement while Fig. 23 provides the maximum base shear recorded for each model. As shown previously in Table 2, the links' web exhibited higher yield and ultimate strengths than the flanges. Consequently, EBF-TO-W links demonstrated greater strength than their EBF-TO-F counterparts. EBF-00-W and EBF-00-F showed an increase of 28 and 20% in the recorded base shear compared to the conventional EBF (EBF-Conv), while EBF-P1-W showed only 5% higher base shear. EBF-B1-W and EBF-B1-F also showed an 8–10% higher base shear compared to EBF-Conv. EBF-P1-F and EBF-P2-F recorded lower base shear compared to EBF-Conv.

The EBF systems are then evaluated under cyclic loading based on AISC 341–16 protocol depicted in Fig. 24. Furthermore, Fig. 25 illustrates how the link rotation is converted into story-level displacements for the EBFs. Figure 26 provides the cyclic response plotted as base shear versus lateral displacements for optimized links, and the cyclic envelopes are

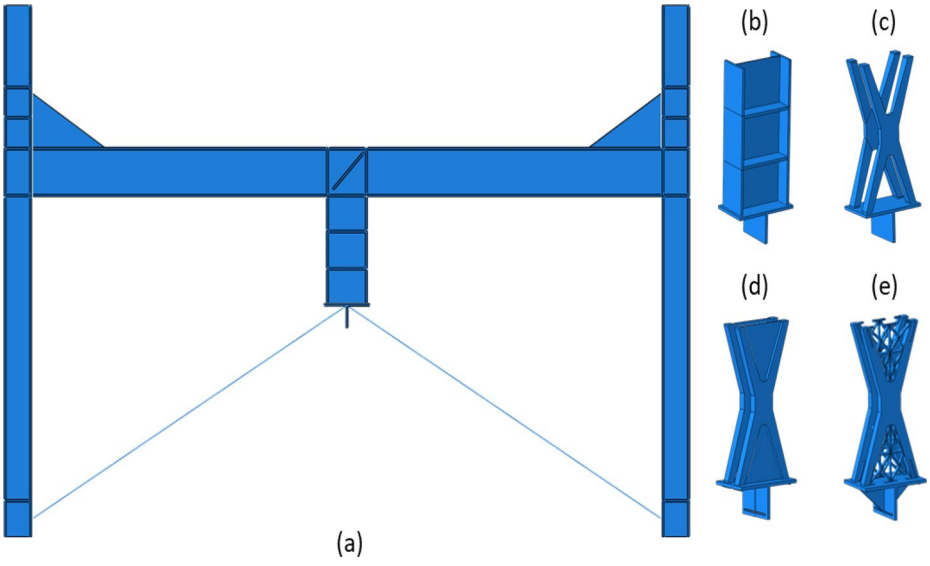

Fig. 21 One-story eccentrically braced frame adopted from (Lian and Su 2017), tested with (**b**) conventional, (**c**) TO-00/01, (**d**)TO-P1/P2 and (**e**)TO-B1 links

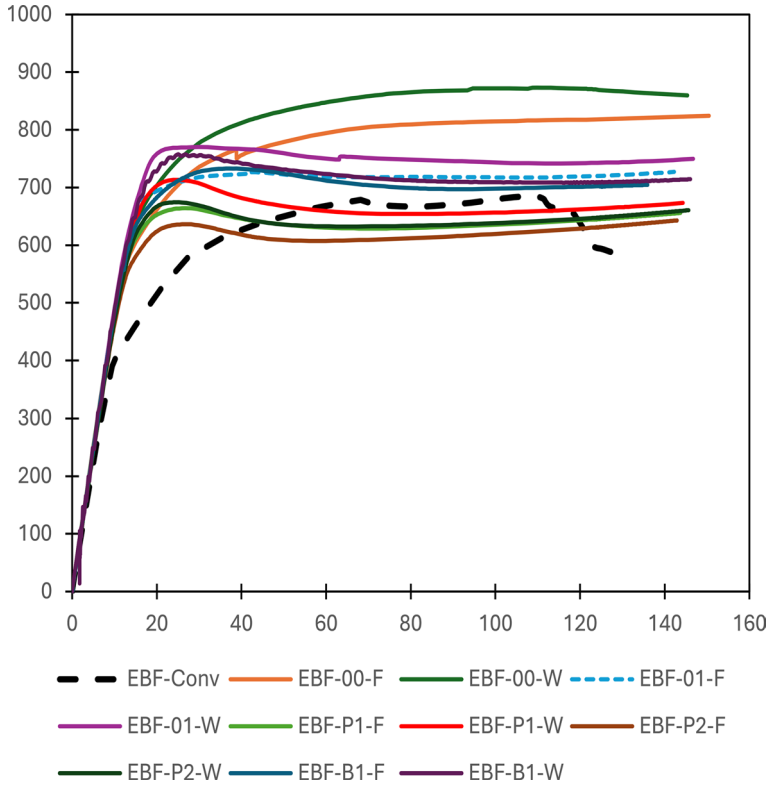

Fig. 22 Base shear versus lateral displacement for EBF

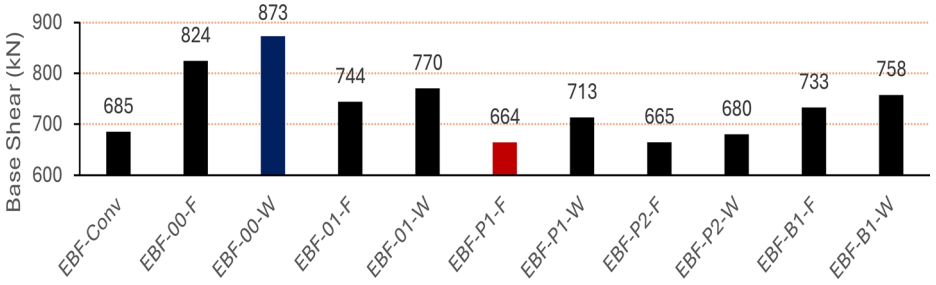

Fig. 23 Maximum base shear (monotonic case) recorded for each model

all compiled in Fig. 27. The maximum base shear recorded for each EBF is summarized in Fig. 28.

In terms of base shear from the cyclic load case, the conventional model (EBF-Conv) sits at the lowest recorded base shear of about 615 kN. EBF-00-W and EBF-00-F showed an increase in maximum base shear ranging from 23% to 30% higher than EBF-Conv, while EBF-01-W and EBF-01-F recorded an increase ranging from 20% to 28% over EBF-

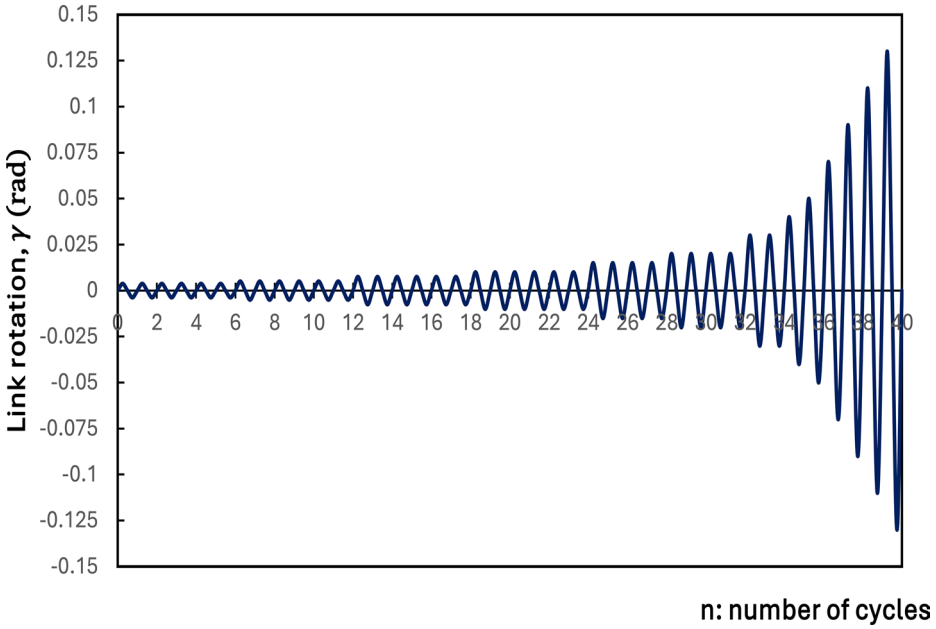

Fig. 24 AISC 341–16 loading sequence

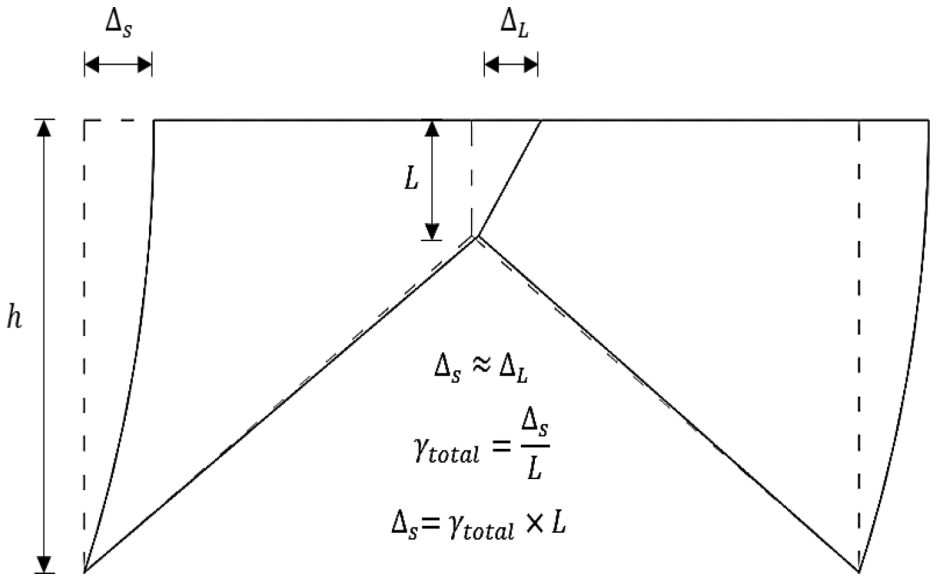

Fig. 25 Converting link rotation to lateral displacement

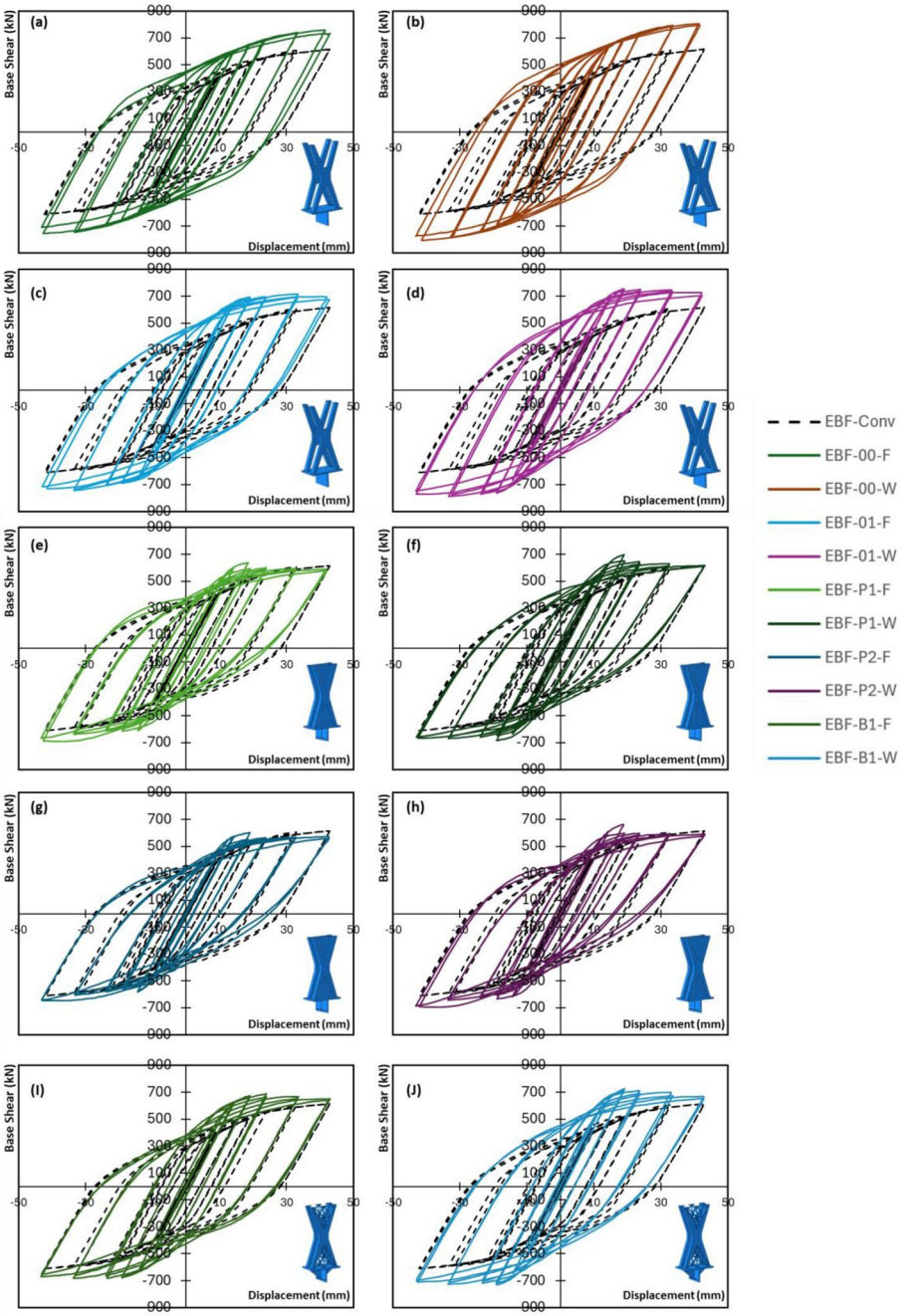

Fig. 26 Base shear versus lateral displacement

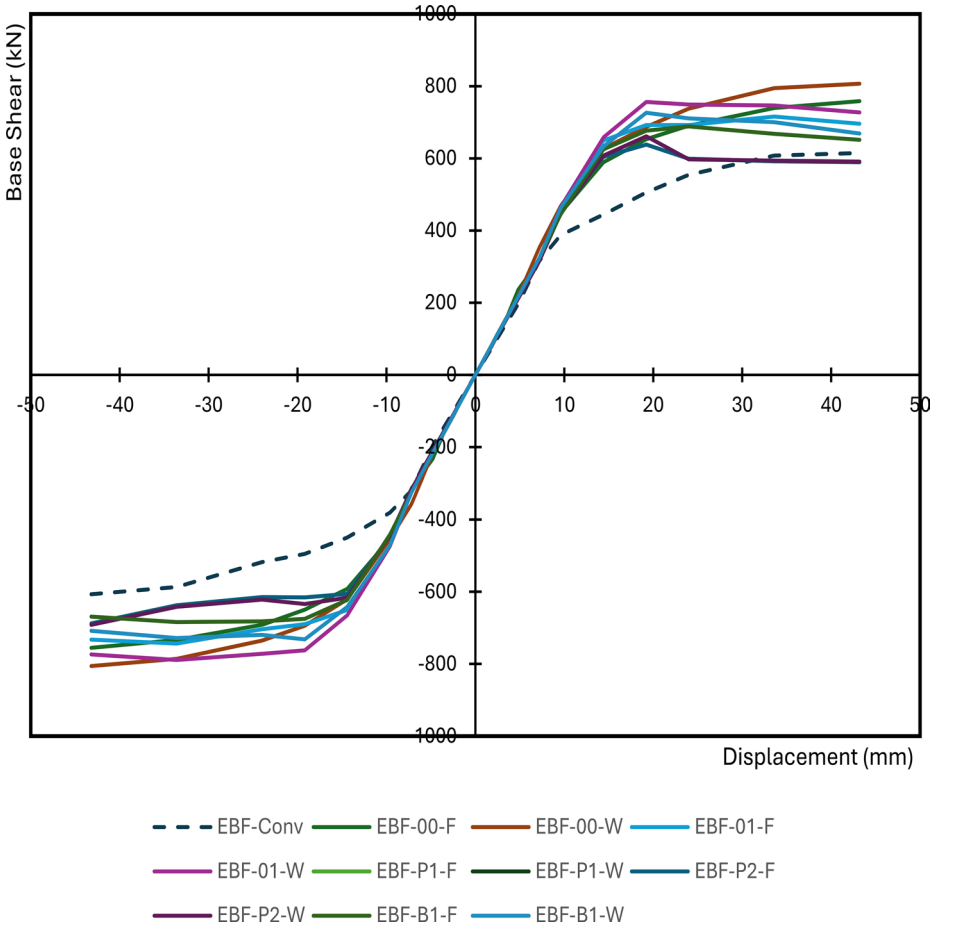

Fig. 27 Base shear versus lateral displacement cyclic envelopes for all EBFs

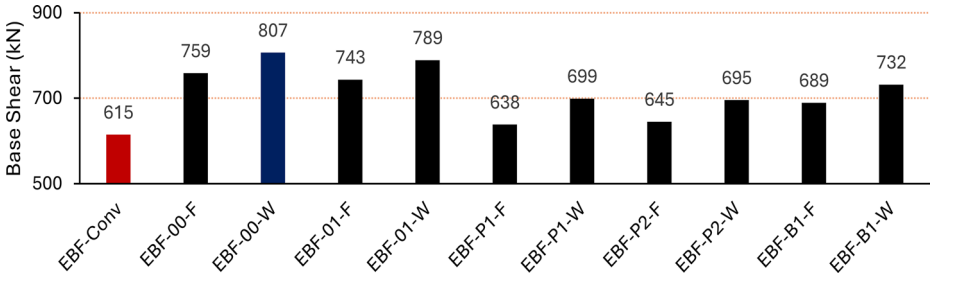

Fig. 28 Maximum base shear (cyclic load case) for all EBFs

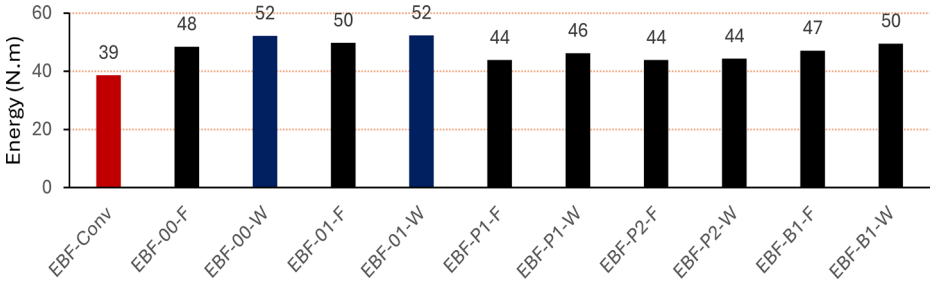

Fig. 29 Energy dissipation (area under cyclic envelope) calculated for all EBFs

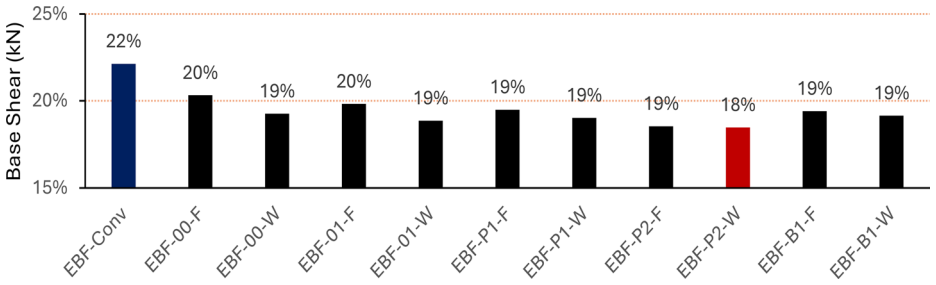

Fig. 30 Equivalent viscous damping coefficient calculated for all EBFs

Conv. EBF-P1-F recorded the lowest increase in base shear, which was still 6% higher than EBF-Conv.

Figure 29 shows the energy dissipation calculated as the area under the cyclic envelope curve. All EBF-TO links showed an increase in the energy dissipation parameter compared to EBF-Conv, ranging from 10% to 35%. EBF-00-W, EBF-01-W and EBF-B1-W were the highest in that respect, with 52, 52 and 50 Joules, ~35% higher than the conventional EBF. EBF-B1-F recorded 20% higher energy dissipation over EBF-Conv under cyclic loading.

Finally, Fig. 30 provides the equivalent viscous damping coefficient. The cumulative damping coefficient was calculated from all the cycles. The optimized links also showed small variations in the calculated damping coefficient as in the case of individual links. The conventional link provided the highest damping coefficient, which can be confirmed by the relative plumpness of the cyclic response noticed in Fig. 26, however, EBF-P2-W, which recorded the lowest damping coefficient, was only 4% behind EBF-Conv. EBF-00-F and EBF-01-F had the second highest damping coefficient behind EBF-Conv, but only 1% higher than EBF-B1-F/W. EBF-P1/P2-F/W had almost the same damping coefficient. The equivalent viscous damping coefficient should not be viewed as the sole indicator of seismic performance. The superior performance of the TO links is better evidenced by their cumulative energy dissipation, and their enhanced strength retention and post-peak stability. The ability to dissipate energy while maintaining higher shear resistance confirms the effectiveness of the optimized topologies for seismic applications.

4 Conclusions

Additive manufacturing (AM) continues to advance the design and fabrication of structural members in the construction industry. By leveraging topology optimization (TO) and wire-and-arc additive manufacturing (WAAM), it is now possible to manufacture shear links with optimized geometries that enhance seismic performance while reducing material usage. This paper introduced a refined numerical approach for optimizing and stiffening shear links used in eccentrically braced frames (EBFs) under monotonic and cyclic loading. The study builds on previous research by incorporating additional stiffening mechanisms, while considering damage and fracture, addressing the performance of topology optimized (TO) links in full-scale EBF systems. The following conclusions summarize the findings:

a) The newly proposed TO links showed superior performance in both individual and EBF configurations when compared to conventional shear links. The stiffened TO links provided increased shear strength, improved energy dissipation, and enhanced stiffness.
b) The optimized TO links consistently demonstrated superior shear strength under monotonic loading, with the baseline topology achieving a 22% increase in capacity compared to the conventional reference link. The introduction of stiffeners and ties in variations such as TO-B1 and TO-B2 further enhanced stress distribution, sustaining load beyond fracture in the X-shaped plates and improving overall ductility.
c) Under cyclic loading, TO-01 and TO-00 exhibited superior energy dissipation reaching 31% improvement over RSL-1. TO-01 recording the highest damping coefficient among the TO links, surpassing the original TO link (TO-00) and nearly matching the conventional RSL-1 link.
d) The study examined the behavior of TO links in full-scale EBF systems, revealing significant improvements over conventional links. The maximum base shear recorded for optimized links ranged from 6% to 35% higher than that of the conventional EBF system. Consistent with the individual TO links' analysis, EBF-01 and EBF-00 links demonstrated the highest base shear and energy dissipation under cyclic loading, while EBF-B1 surpassed EBF-P1, EBF-P2 and EBF-Conv, underscoring their effectiveness as high-performance shear links.
e) The modified TO links addressed major concerns associated with manufacturability. The study proposed a hybrid approach where WAAM is used selectively for reinforcement rather than full fabrication, reducing issues related to distortion and residual stresses. Additionally, CNC-cut X-plates combined with strategically placed stiffeners proposes a more practical and effective alternative.
f) Unlike conventional I-shaped shear links, which often experience shear buckling in the web, the optimized TO links exhibited different failure modes. Most failures in non-stiffened configurations were attributed to tensile rupture at stress-concentrated regions. The inclusion of plates and braces in TO-P1/P2 and TO-B1/B2 effectively mitigated this issue, redistributing stresses and delaying failure.

In conclusion, this research highlights new advancements in the design of shear links for eccentrically braced frames. By integrating topology optimization with strategic stiffening techniques, the proposed TO links achieve superior seismic performance while maintaining practical manufacturability. The results demonstrate the numerical feasibility of topology-

optimized shear links, suggesting they offer a promising alternative to conventional seismic energy dissipation mechanisms. While this study demonstrates the potential of stiffened TO links, it is essential to acknowledge the numerical nature of these findings. The reported performance is predicated on the accuracy of the adopted constitutive and damage models calibrated for Q345 steel. Furthermore, the analysis assumed isotropic mechanical properties for the WAAM-fabricated stiffeners, idealizing the interface between the printed material and the base plate. In physical applications, WAAM processes may introduce residual stresses, porosity, or geometric imperfections that could influence fatigue life and fracture initiation. Moreover, future studies should address the behavior of TO links in multi-story structures, building on the investigations presented in this paper.

Acknowledgements The authors would like to acknowledge the British University in Egypt (BUE) and AMCL lab at the American University in Cairo (AUC) for the support of this research.

Author contribution Yasser N. Saleh: Writing – original draft, Visualization, Methodology, Investigation, Formal analysis. Sherif A. Mourad: Writing – review & editing, Supervision. Hanadi G. Salem: Writing – review & editing, Supervision. Amr M. Ibrahim: Writing – review & editing, Supervision, Conceptualization.

Funding Open access funding provided by The Science, Technology & Innovation Funding Authority (STDF) in cooperation with The Egyptian Knowledge Bank (EKB). This research received no specific grant from any funding agency in the public, commercial, or not-for-profit sectors.

Data availability The datasets are available from the corresponding author on reasonable request.

Declarations

Conflict of interest The authors declare that they have no conflict of interest.

References

Abe T, Sasahara H (2019) Layer geometry control for the fabrication of lattice structures by wire and arc additive manufacturing. Addit Manuf 28:639–648

Avecillas JA, Eatherton MR (2020) Controlling out-of-plane buckling in shear-acting structural fuses through topology optimization. J Stru Eng 146(7):04020132

Baglivo L, Avallone G, Caso M, D'Arcangelo S, Benni AA, Laghi V, Arrè L, Gasparini G, Palermo M, Petrò S, Xu T, Previtali B (2024) Design and prototyping wire arc additively manufactured aluminum alloy lattice structures. Int J Adv Manuf Technol 1–18

Baqershahi MH, Ayas C, Ghafoori E (2024) Design optimisation for hybrid metal additive manufacturing for sustainable construction. Eng Struct 301:117355

Bendsoe MP, Sigmund O (2013) Topology optimization: theory, methods, and applications. Springer Science & Business Media

Bendsøe MP, Sigmund O (1999) Material interpolation schemes in topology optimization. Arch Appl Mech 69(9):635–654

Brunesi E, Nascimbene R (2025) Fibre-based model for dynamic analysis of high-rise mega-braced frame-core building systems. Eng Struct 343:120988
Bustos F, Hinojosa J, Olivos A (2025) Numerical characterization and experimental validation of steel plate shear yielding damper. In: Structures, vol 72. Elsevier, p 108215
Ebrahimi Majumerd MJ, Mohammadi Dehcheshmeh E, Broujerdian V, Laghi V, Palermo M (2023) Introducing a base-rocking dual-core braced-frame system equipped with vertical buckling-restrained fuses. Bull Earthquake Eng 21(14):6453–6476
Esteghamati MZ, Farzampour A (2020) Probabilistic seismic performance and loss evaluation of a multi-story steel building equipped with butterfly-shaped fuses. J Educ Chang Constructional Steel Res 172:106187
Farzampour A (2021) Structural behavior prediction of the butterfly-shaped and straight shear fuses. In: Structures, vol 33. Elsevier, pp 3964–3972
Farzampour A, Eatherton MR (2019) Yielding and lateral torsional buckling limit states for butterfly-shaped shear links. Eng Struct 180:442–451
Gardner L, Li J, Meng X, Huang C, Kyvelou P (2024) I-section steel columns strengthened by wire arc additive manufacturing-concept and experiments. Eng Struct 306:117763
Giuliani G, Andreotti R, Tondini N (2024) Hybrid simulation of a steel frame with dissipative replaceable link frames. Bull Earthquake Eng 22(8):4023–4053
Goshtaei SM, Moradi S, Hossain KMA (2024) Multi-objective optimization of energy-dissipating steel plate fuse links using response surface method. In: Structures, vol 62. Elsevier, p 106224
Gu J, Chen Z, Long K, Wang Y (2024) Nonlinear fatigue damage constrained topology optimization. Comput Methods Appl Mech Eng 429:117136
Guo W, Wang X, Yu Y, Chen X, Li S, Fang W et al (2020) Experimental study of a steel damper with X-shaped welded pipe halves. J Educ Chang Constructional Steel Res 170:106087
Hancock JW, Mackenzie AC (1976) On the mechanisms of ductile failure in high-strength steels subjected to multi-axial stress-states. J Mech Phys Solids 24(2–3):147–160
Huang C, Kyvelou P, Zhang R, Britton TB, Gardner L (2022) Mechanical testing and microstructural analysis of wire arc additively manufactured steels. Mater. Des 216:110544
Hui C, Zhou Z, Li Y, Jiao Y, Hai R (2022) Quasi-static cyclic loading experiment and analysis of double-side slotted steel tube shear damper. Arch Civ Mech Eng 23(1):45
Kanvinde AM, Deierlein GG (2006) Void growth model and stress modified critical strain model to predict ductile fracture in structural steels. J stru Eng
Khosravani MR, Bieler S, Weinberg K, Reinicke T (2025) Mechanical fracture of lattice structures fabricated by selective laser sintering. Arch Civ Mech Eng 25(2):1–12
Kloft H, Schmitz LP, Müller C, Laghi V, Babovic N, Baghdadi A (2023) Experimental application of robotic wire-and-arc additive manufacturing technique for strengthening the I-beam profiles. Buildings 13(2):366
Kyvelou P, Slack H, Mountanou DD, Wadee MA, Britton TB, Buchanan C, Gardner L (2020) Mechanical and microstructural testing of wire and arc additively manufactured sheet material. Mater. Des 192:108675
Laghi V, Arrè L, Gasparini G, Trombetti T, Palermo M (2025 January) Design strength parameters of dot-by-dot wire-and-arc additively manufactured stainless steel bars. In: Structures, vol 71. Elsevier, p 107857
Laghi V, Palermo M, Tonelli L, Gasparini G, Girelli VA, Ceschini L, Trombetti T (2022) Mechanical response of dot-by-dot wire-and-arc additively manufactured 304L stainless steel bars under tensile loading. Construct Building Mater 318:125925
Lee CH, Ju YK, Min JK, Lho SH, Kim SD (2015) Non-uniform steel strip dampers subjected to cyclic loadings. Eng Struct 99:192–204
Li S, Xie X, Cheng C, Tian Q (2020) A modified Coffin-Manson model for ultra-low cycle fatigue fracture of structural steels considering the effect of stress triaxiality. Eng Fract Mech 237:107223
Li Y, Yu S, Chen Y, Yu R, Shi Y (2020) Wire and arc additive manufacturing of aluminum alloy lattice structure. J Retailing Manuf Processes 50:510–519
Lian M, Su M (2017) Seismic performance of high-strength steel fabricated eccentrically braced frame with vertical shear link. J Educ Chang Constructional Steel Res 137:262–285
Liao FF, Wang W, Chen YY (2011) Experimental study to calibrate monotonic micromechanics-based fracture models of Q345 steel. Adv Mater Res-Switz 261:545–550
Liu C, Xu T, Mao H, Li K, Jing C, Liu B et al (2023) Quasi-static compressive behaviors of large-size titanium lattice sandwich structure based on pulse hot-wire arc additive manufacturing. Mat. Sci. Eng. A 868:144787
Liu XG, Fan JS, Liu YF, Yue QR, Nie JG (2017) Experimental research of replaceable Q345GJ steel shear links considering cyclic buckling and plastic overstrength. J Educ Chang Constructional Steel Res 134:160–179
Louzai A, Abed A (2025) A simplified design procedure for seismic retrofitting of RC frames with setbacks using eccentric steel braces having vertical shear link elements. Bull Earthquake Eng 1–34

Luo Z, MacRae G, Xue J, Pettinga D (2024) Benefit of structural access panels (SAP) for post-earthquake structural health monitoring. Bull Earthquake Eng 22(4):1881–1907
Majdak M, Baranowski P, Małachowski J (2024) Numerical studies of the energy absorption capacities and deformation mechanisms of 2D cellular topologies. Arch Civ Mech Eng 24(2):111
Mazzotta V, Brunesi E, Nascimbene R (2017) Numerical modeling and seismic analysis of tall steel buildings with braced frame systems. Periodica Polytech Civ Eng 61(2):196–208
Nascimbene R (2013) An arbitrary cross section, locking free shear-flexible curved beam finite element. Int J Comp Met Engi Sci Mech 14(2):90–103
Nascimbene R (2024) Investigation of seismic damage to existing buildings by using remotely observed images. Eng Fail Anal 161:108282
Nascimbene R, Bianchi F, Brunesi E, Bellotti D (2025) A global performance-based seismic assessment of a retrofitted hospital building equipped with dissipative bracing systems. Buildings 15(22):4022
Nguyen TN, Eatherton MR (2023a) Computational and experimental study of structural fuses optimized to resist buckling. J Educ Chang Constructional Steel Res 201:107688
Nguyen TN, Eatherton MR (2023b) Development of the tied butterfly shape for structural fuses. Eng Struct 297:116999
Ramonell C, Chacon R (2021) On the topological optimization of horizontal links in eccentrically braced frames. J Educ Chang Constructional Steel Res 185:106887
Rice JR, Tracey DM (1969) On the ductile enlargement of voids in triaxial stress fields. J Mech Phys Solids 17(3):201–217
Saleh YN, Mourad SA, Ibrahim AM (2024) Topology optimization of vertical shear links in eccentrically braced frames. In: Structures, vol 66. Elsevier, p 106821
Sigmund O, Maute K (2013) Topology optimization approaches: a comparative review. Struct. Multidiscip. Optim 48(6):1031–1055
Sullivan TJ, Calvi PM, Nascimbene R (2013) Towards improved floor spectra estimates for seismic design. Earthquakes Struct 4(1):109–132
Wang Z, Hou Y, Huang C, Han Q, Zong L, Chen MT et al (2024) Experimental study and constitutive modelling of wire arc additively manufactured steel under cyclic loading. J Educ Chang Constructional Steel Res 213:108420
Wijesundara KK, Nascimbene R, Sullivan TJ (2011) Equivalent viscous damping for steel concentrically braced frame structures. Bull Earthquake Eng 9:1535–1558
Xie Z, Wang W, Yao Z (2025) Experiments and modeling of the combined tension-shear ultra-low-cycle fatigue of structural steel sheet regarding loading histories. Eng Fract Mech 313:110682
Xu H, Liu C, Mao H, Bai F, Xu T (2024) Strengthening nodes to obtain high-strength pyramid lattice structure by using wire arc additive manufacturing method. J Retailing Manuf Processes 117:125–133
Yang J, Wadee MA, Gardner L (2025) Strengthening of steel I-section beams by wire arc additive manufacturing-concept and experiments. Eng Struct 322:119113
Yu Z, Ding D, Pan Z, Li H, Lu Q, Fang X (2021) A strut-based process planning method for wire arc additive manufacturing of lattice structures. J Retailing Manuf Processes 65:283–298
Yu Z, Pan Z, Ding D, Rong Z, Li H, Wu B (2022) Strut formation control and processing time optimization for wire arc additive manufacturing of lattice structures. J Retailing Manuf Processes 79:962–974
Yue K, Xu L, Liu J, Fan L, Xu L (2024) Energy dissipation evaluation of butterfly-shaped steel plate shear keys under different loading protocols. In: Structures, vol 60. Elsevier, p 105893
Zhan J, Zhu X, Zhu B, Liu M (2025) Fatigue reliability-based topology optimization of compliant mechanisms considering material uncertainties. Struct. Multidiscip. Optim 68(5):1–17
Zhang H, Huang J, Liu C, Ma Y, Han Y, Xu T et al (2020) Fabricating pyramidal lattice structures of 304 L stainless steel by wire arc additive manufacturing. Materials 13(16):3482
Zhu B, Wang T, Zhang L (2018) Quasi-static test of assembled steel shear panel dampers with optimized shapes. Eng Struct 172:346–357

Authors and Affiliations

Yasser N. Saleh[1,2] · Sherif A. Mourad[2] · Hanadi G. Salem[3] · Amr M. Ibrahim[1]

✉ Yasser N. Saleh
Yasser.Nasr@bue.edu.eg

Sherif A. Mourad
smourad@eng.cu.edu.eg

Hanadi G. Salem
hgsalem@aucegypt.edu

Amr M. Ibrahim
amr.ibrahim@bue.edu.eg

[1] Civil Engineering Department, Faculty of Engineering, British University in Egypt, Cairo 11837, Egypt

[2] Structural Engineering Department, Faculty of Engineering, Cairo University, Giza 12613, Egypt

[3] Mechanical Engineering Department, Faculty of Engineering, American University in Cairo, New Cairo 11835, Egypt